The Effect of Lattice Strain in Electrochemical Oxidations Catalyzed by Au-PdPt Core-shell Octahedral Nanoparticles

Author: Momo Yaguchi

Persistent link: http://hdl.handle.net/2345/2928

This work is posted on eScholarship@BC,
Boston College University Libraries.

Boston College Electronic Thesis or Dissertation, 2012

Copyright is held by the author, with all rights reserved, unless otherwise noted.

Boston College

The Graduate School of Arts and Sciences

Department of Chemistry

THE EFFECT OF LATTICE STRAIN IN ELECTROCHEMICAL OXIDATIONS CATALYZED BY Au-PtPd CORE-SHELL OCTAHEDRAL NANOPARTICLES

a thesis

by

MOMO YAGUCHI

submitted in partial fulfillment of the requirements for the degree

of

Master of Science

December 2012

@ copyright by MOMO YAGUCHI

2012

ABSTRACT

The effect of lattice strain in electrochemical oxidation catalyzed by Au-PtPd core-shell octahedral nanoparticles

Momo Yaguchi

Thesis Advisor: Professor Chia-kuang Tsung

Pt-based alloy and core-shell nanoparticles have been intensively studied to regulate its size and shape. It has known that these nanoparticles show enhanced catalytic activity in various important fields such as heterogeneous catalysis, and electrochemical energy storage including fuel cells and metal-air batteries.

Here, we report a facile hydrothermal synthesis of sub-10 nm PdPt alloy and sub-20 nm Au@PdPt core-shell structures. By using a mild reducing agent in aqueous solution, metal precursors are co-reduced. Specific gases are introduced during the synthesis to optimize the reaction conditions. The PdPt alloy and Au@PdPt core-shell nanostructures were characterized and confirmed by TEM, HRTEM, EDS, ICP-OES and XRD. The resulting PdPt and Au@PdPt particles are monodispersed single crystalline and octahedral shape enclosed by (111) facets. The electrocatalytic activity for the oxidation of formic acid was tested. It was found that the catalytic activity toward the formic acid oxidation of Au@PdPt core-shell particles were much higher than those of PdPt alloy particles. In addition, Pt-rich compositions were the most active in both PdPt alloy and Au@PdPt core-shell nanoparticles. Further studies on thinner alloy-shell core-shell nanoparticles reveal that there is a volcano-curve relationship between the

lattice strain strength related to alloy-shell thickness and the catalytic performance. It is proposed that there are three key parameters that can determine the catalytic activity: the alloy composition, the presence of the gold core, and the thickness of alloy-shell.

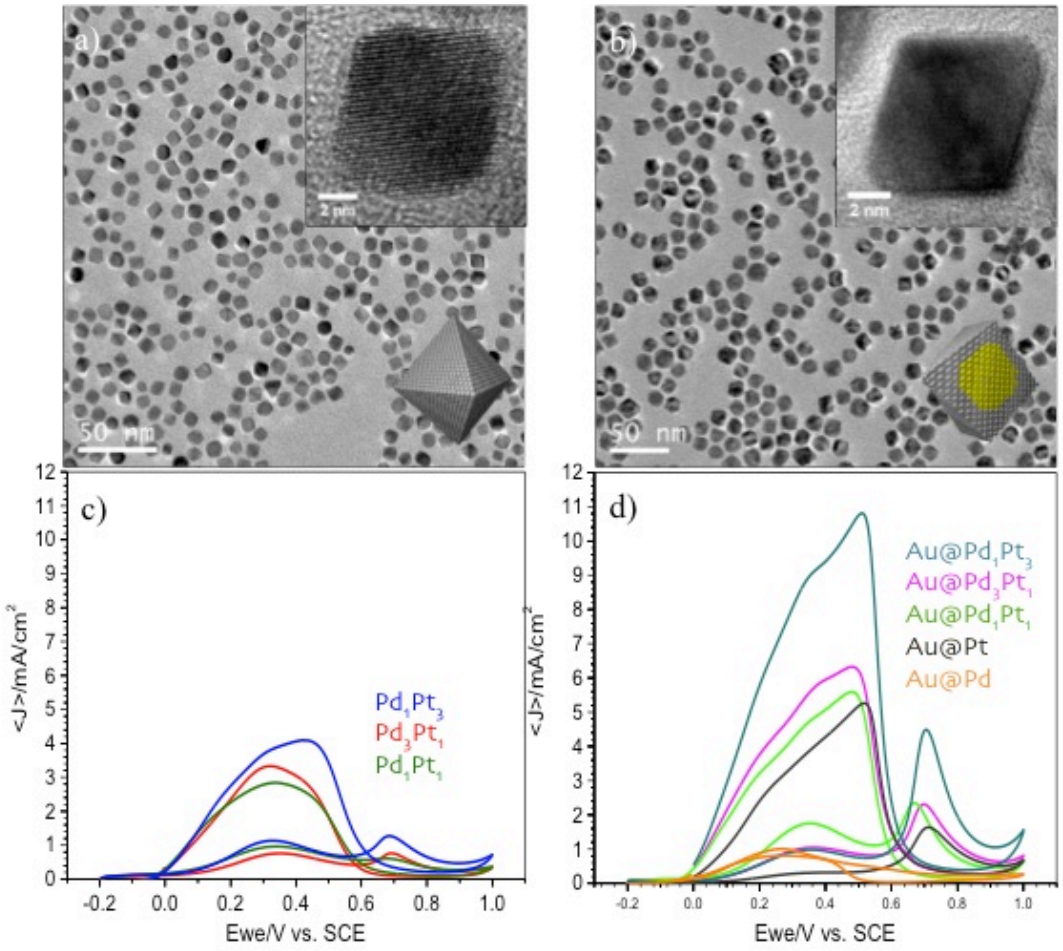

Representative TEM/HRTEM images and the corresponding formic acid oxidation activities for a, c) PdPt alloy octahedral nanoparticles b, d) Au@PdPt core-shell octahedral nanoparticles.

TABLE OF CONTENTS

List of Figures……... iv

List of Tables……...…vii

List of Schemes……viii

CHAPTER 1: INTRODUCTION……1

1.1 Noble Metal Nanoparticles…….....1

1.2 Nanoparticles for Electrochemical Energy Storage…….2

1.3 Alloy and Core-shell Bimetallic Nanoparticles……..3

1.4 Research Motivation…….…5

CHAPTER 2: EXPERIMENTAL PROCEDURES…….12

2.1 Chemicals……...….12

2.2 Synthetic Procedure……...….12

2.2.1 Synthesis of PdPt Alloy Octahedral Nanoparticles……..12

2.2.2 Preparation of Gold Seeds……13

2.2.3 Synthesis of Au@PdPt Core-shell Octahedral Nanoparticles..... 14

2.3 Sample Preparation for Characterization……...…….15

2.3.1 Sample Preparation for TEM and EDS……...…..15

2.3.2 Sample Preparation for ICP-OES…….15

2.3.3 Sample Preparation for Powder-XRD…….....16

2.4 Electrochemical Measurement Procedure……...…16

2.4.1 Blank Scan……16

2.4.2 Formic Acid Oxidation…….17

2.4.3 CO stripping…….17

2.5 Instrumentation……...18

CHAPTER 3: CHARACTERIZATION AND ANALYSIS…..……19

3.1 Size and Shape Characterization by TEM and HRTEM……..…..19

3.1.1 Gold Seeds……19

3.1.2 PdPt Alloy Octahedral Nanoparticles……...20

3.1.3 Au@PdPt Core-shell Octahedral Nanoparticles…….…..……21

3.2 Elemental Analysis by EDS and ICP-OES…….……22

3.2.1 PdPt Alloy Octahedral Nanoparticles……...22

3.2.2 Au@PdPt Core-shell Octahedral Nanoparticles……...22

3.3 Crystallographic Analysis by Powder-XRD……...…....23

3.3.1 PdPt Alloy Octahedral Nanoparticles……...23

3.3.2 Au@PdPt Core-shell Octahedral Nanoparticles...……....25

3.4 XRD (220) Pattern Analysis……...…26

3.4.1 PdPt Alloy Octahedral Nanoparticles……...26

3.4.2 Au@PdPt Core-shell Octahedral Nanoparticles.....27

3.5 PdPt Alloy Octahedral Nanoparticle Growth Mechanism……..28

3.5.1 Reducing Agent Type……...28

3.5.2 Gas Type…….……..30

3.5.3 Sodium Citrate Amount and Gas Type…….……30

3.5.4 Particle Formation Scheme…….……..32

CHAPTER 4: ELECTROCHEMICAL MEASUREMENTS…..……34

4.1 Formic Acid Oxidation Reaction……...….34

4.2 Electrochemical Measurements……..……35

4.2.1 Blank Scan……35

4.2.2 CO stripping…….….37

4.2.3 Formic Acid Oxidation……40

CHAPTER 5: DISCUSSION……..43

5.1 Thinner shell C1S2 Au@PdPt Core-shell Octahedral Nanoparticles..…...43

5.1.1 Characterization……...…….44

5.1.2 Electrochemical Measurements……...…….45

5.1.3 XRD (220) Pattern Analysis……..…48

5.2 The Effect of Lattice Strain for Catalytic Activity…..…….....51

CHAPTER 6: CONCLUSION……52

LIST OF FIGURES

Figure 1 Examples of bimetallic nanoparticles……2

Figure 2.1 Picture of the growth solution color changes before and after the heating……15

Figure 3.1 TEM image of as-synthesized gold seeds……..19

Figure 3.2 TEM and the corresponding HRTEM images for PdP alloy nanoparticles……..20

Figure 3.3 TEM and the corresponding HRTEM images for Au@PdPt core-shell nanoparticles……..21

Figure 3.4 XRD patterns for PdPt alloy octahedral nanoparticles……..24

Figure 3.5 XRD patterns for Au@PdPt core-shell octahedral nanoparticles……..25

Figure 3.6 XRD (220) patterns of PdPt alloy nanoparticles with three different compositions……..27

Figure 3.7 XRD (220) patterns of Au@PdPt core-shell nanoparticles with three different alloy-shell compositions……..28

Figure 3.8 Pd_1Pt_1 alloy particles with sodium citrate and the mixture of sodium citrate and ascorbic acid…….29

Figure 3.9 Pd_1Pt_1 alloy particles with introducing argon, air and oxygen gases during the synthesis……30

Figure 3.10 TEM images for Pd_1Pt_1 alloy particles either with argon or oxygen, changing the amount of sodium citrate……..31

Figure 4.1 Reaction pathways and representative cyclic voltammograms for

indirect and direct oxidation of formic acid……...35

Figure 4.2 Blank scan of electrode used in the measurements for PdPt alloy and Au@PdPt core-shell nanoparticles……35

Figure 4.3 Blank scan of electrode with PdPt alloy and Au@PdPt core-shell nanoparticles with three different alloy compositions……...36

Figure 4.4 CO stripping peaks for PdPt alloy and Au@PdPt core-shell nanoparticles……..38

Figure 4.5 The linear relationship between PdPt alloy composition and the CO stripping peak position……...39

Figure 4.6 Formic acid oxidation activity for PdPt alloy and Au@PdPt core-shell nanoparticles……..40

Figure 4.7 Formic acid oxidation activity summary for octahedral PdPt alloy and Au@PdPt core-shell nanoparticles…….42

Figure 5.1 TEM images and their corresponding FOR activity of PdPt alloy and Au@PdPt core-shell octahedral nanoparticles……...43

Figure 5.2 TEM images for thinner alloy-shell (C1S2) Au@PdPt core-shell octahedral nanoparticles…….44

Figure 5.3 CO stripping cyclic voltammograms for C1S2 and C1S10 Au@PdPt core-shell octahedral nanoparticles……...45

Figure 5.4 FOR activity comparison of C1S2 and C1S10 Au@PdPt core-shell octahedral nanoparticles…….46

Figure 5.5 A chart to compare the FOR activity of PdPt alloy, C1S10 Au@PdPt and C1S2 Au@PdPt core-shell nanoparticles with three different alloy compositions……..47

Figure 5.6 XRD (220) patters of PdPt alloy and C1S10 Au@PdPt core-shell octahedral nanoparticles…….48

Figure 5.7 XRD (220) pattern comparisons of C1S2 and C1S10 Au@PdPt core-shell nanoparticles for each alloy-shell composition…….49

Figure 5.8 Volcano-like relationship between the FOR catalytic activity and the alloy-shell thickness……...51

LIST OF TABLES

Table 3.1 Elemental analysis results for PdPt alloy nanoparticles with three different compositions……...22

Table 3.2 Elemental analysis results PdPt alloy-shell of Au@PdPt core-shell nanoparticles with three different compositions……23

Table 3.3 XRD 2Θ values for each crystal facet of PdPt alloy nanoparticles….24

Table 3.4 The d-space length for PdPt alloy nanoparticles……...24

Table 3.5 XRD 2Θ values for each crystal facet of Au@PdPt core-shell nanoparticles……..26

Table 3.6 The d-space length for gold seed and Au@PdPt core-shell nanoparticles……..26

Table 4.1 CO peak position and the corresponding surface area……...37

Table 4.2 The list of FOR activity of PdPt alloy and Au@PdPt core-shell octahedral nanoparticles…… 41

Table 5.1 Elemental analysis results for PdPt alloy-shell of C1S2 Au@PdPt core-shell nanoparticles with three different compositions……...45

Table 5.2 The d-space value changes of PdPt alloy-shell in C1S10 and C1S2 Au@PdPt core-sell octahedral nanoparticles……50

LIST OF SCHEMES

Scheme 2.1 Schematic illustration of the procedure used for preparing PdPt alloy octahedral nanoparticles…….13

Scheme 2.2 Schematic illustration of the procedure used to synthesize Au@PdPt core-shell octahedral nanoparticles……14

Scheme 3.1 Schematic illustration of octahedral PdPt alloy nanoparticle growth mechanism…….32

Scheme 3.2 Schematic illustration of octahedral PdPt alloy nanoparticle formation mechanism: 1) with strong reducing agent 2) less oxygen in the system (argon is introduced) 3) more oxygen in the system (oxygen is introduced)…….33

Scheme 5.1 Schematic illustration of lattice expansion of PdPt alloy-shell in Au@PdPt core-shell octahedral nanoparticles……..50

CHAPTER 1

Introduction

1.1 Noble Metal Nanoparticles

Noble and Platinum group metal nanoparticle catalysts like gold, silver, platinum, palladium, and rhodium play an important role in industrial chemical reactions including hydrogenations, carbon monoxide oxidation, organic coupling and more recently in fuel cell reactions like alcohol oxidations and oxygen reduction. However, their rarity makes running these reactions expensive. Due to the need to develop more active and cost-effective catalysts, bimetallic nanoparticle synthesis has become an attractive research direction. As shown in Figure 1, bimetallic nanoparticles consist of two different metals combined in a variety of ways into a single nanoparticle. Alloyed nanoparticles contain two different metals incorporated into a single particle. Core-shell nanoparticles consist of a metal core with a different metal shell, and heterostructures involve two distinct nanoparticles joined together.[1] There are three main benefits bimetallic nanoparticles have over their monometallic counterparts. First, a second metal can introduce added stability by preventing particle aggregation during reactions and increasing thermal stability.[2,3] Secondly, incorporating inexpensive metal into a noble metal nanoparticle can greatly reduce catalyst cost by conserving the use of precious metals.[4,5] Finally and most importantly, a second metal can modify the structural and electronic properties of a nanoparticle leading to enhanced catalytic activity.[6] Structural enhancement can be caused by differences in lattice parameters of the metals which change the surface energies. Activity increased arising from electronic effects can be

attributed to changes in the d-band center of the material as the two metals interact with each other. A changing of the d-band center can increase or decrease reactant absorption energies leading to higher activities because of a difference in populating and anti-bonding states.[7]

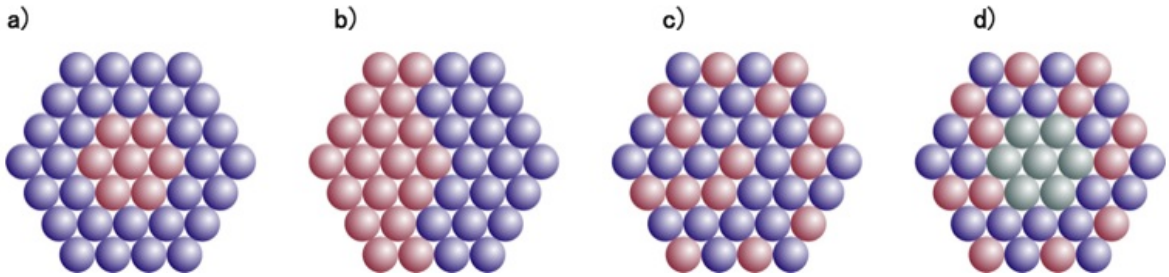

Figure 1 Examples of bimetallic nanoparticles. a) Core-shell b) Heterostructure c) Alloy d) Alloy Core-shell.

1.2 Bimetallic Nanoparticles for electrochemical Energy Storage

Bimetallic nanoparticles have great potential as highly active catalysts in fuel cells and metal-air batteries.[8-10] Fuel cells and metal air batteries are currently being researched as power sources for a variety of electronic devices including, cars, laptops, PDAs, and small machinery.[11] Fuel cells stand to be long-lasting, clean, and renewable sources of electricity for these applications. However, sluggish reaction kinetics at the anode and cathode as well as high catalyst cost currently prohibit most fuel cells from main-stream industrial usage. A carefully engineered bimetallic catalyst can solve these problems by reducing expensive noble metal usage, while increasing activity and catalyst stability.

Difficulties in bimetallic nanoparticle synthesis include lack of size and shape

control. Controlling the morphology of nanoparticles is crucial in optimizing catalyst activity as different crystal facets can have widely different activities for various reactions.[12,13] Likewise, synthesizing bimetallic catalysts should not come at the cost of electrochemically active surface area. Two common synthetic methods are co-reduction[14] and seeded-growth.[15] Co-reduction is a single step process in which both metals are introduced into the reaction. Differences in the reduction potentials of the metals lead to various types of bimetallic particles. If the reduction potentials are similar, alloyed particles are more likely to form. If they are different, core-shell particles can form with the more easily reduced metal occupying the core. Seeded-growth reactions are done in two steps. In the first reaction, a single metal is reduced to form a core. In the second step these seeds are introduced with the second metal precursor to form bimetallic particles. This synthetic route generally forms core-shell particles with epitaxially grown shells, but can form other types based on reduction potentials and galvanic replacement.

1.3 Alloy and Core-shell Nanoparticles as Electrocatalysts

Platinum is the most active and durable catalyst and has traditionally been used for cathodic and anodic reactions such as oxygen reduction reaction, methanol oxidation reaction, ethanol oxidation reaction and formic acid oxidation reaction for fuel cells. While it possesses excellent activity, high costs associates with the loading of Pt for fuel cells and the limited supply have hindered the wide commercialization of fuel cells. A number of challenges have been developed to reduce the amount of Pt usage without losing the activity. Platinum nanoparticles with controlled morphologies such as

tetrahedral,[16] cubic,[17-19] and truncated octahedral[20] structures have been demonstrated as highly active catalyst. Also, the synthetic route to produce alloy,[21] core-shell,[17] branched[23] and hybrid[24] Pt-based catalysts has been studied intensively. Among all, one of the most common and promising approaches is to engineer shape, size, and composition of Pt-based bimetallic nanoparticles. Studies have shown the activity of bimetallic nanoparticles to be much greater than pure single metal nanoparticles.[25-30]

Palladium is also an attractive fuel cell catalyst.[31-34] It is relatively inexpensive as compared to the widely used platinum catalysts, and is at least 50 times more abundant than platinum in the Earth. Pd-based nanostructures have shown potential for alcohol oxidation,[35] formic acid oxidation,[36] and oxygen reduction reactions.[37] It is particularly suited for a direct formic acid fuel cell as the reaction follows a direct pathway and does not have a poisoning CO intermediate stage.

Alloying platinum with other metals like palladium has recently been shown to drastically increase activity and provide stability toward various fuel cell[38-44] and organic reactions.[45-47] Novel Pd-Pt alloy catalysts are promising candidates for fuel cells reactions because of the lower cost, greater abundance of Pd and long-term stability. One advantage of choosing Pd-Pt alloy particles is both platinum and palladium have a face-centered cubic (fcc) structure with almost the same unit cell length.

Gold can serve as a very stable core allowing for more precise size and morphological control as opposed to other potential cores.[48-50] The increase in activity can be partly explained due to their lattice mismatch of 4.6%. This difference causes the gold core to exert strain onto shell metal leading to more favorable surface energies. Also, differences in the d-band center of platinum and palladium, and gold has been shown to

favorably affect the electronic properties of core-shell Au@Pt and Au@Pd particles leading to further increase in activity.[51-53]

Because of the varying effects that second metal or metal cores can have on the activity of the alloy and shell metal, and the relatively little research done involving morphologically controlled alloy and core-shell particles, it is attractive to synthesize various morphologies of Pt-based alloy and core-shell structures. As Markovic[36] has shown for Pt_3Ni crystal facets, alloying nickel into platinum will increase activity toward oxygen reduction for the (100) (111) and (110) crystal facets, but the extent of the increase varies greatly between the 3 surfaces, with the (111) crystal facet showing a much greater increase in activity than the (110) and (100) facets. Based on these results it can be prudent to control the morphologies of alloy and core-shell nanoparticles as best as possible to determine the most active crystal facet.

1.4 Research Motivation

In this study, first alloy nanoparticles that incorporate palladium into platinum were synthesized by a simple co-reduction hydrothermal method in aqueous phase. Then, core-shell nanoparticles consisting of a gold core and a platinum-palladium alloy-shell were synthesized by a two-step seeded-growth hydrothermal method in aqueous phase. Tuning the ratio of the platinum to the palladium precursor for alloy particles, and the gold seeds to the alloy precursors for core-shell particles is important as well as controlling the amount of reducing agent, and utilizing the appropriate gases during the synthesis. 9 nm PdPt alloy and 16 nm Au@PdPt core-shell octahedral nanoparticles were

obtained. The particles were characterized using TEM, HRTEM, EDS, ICP-OES, and XRD. The catalytic performance of the particles was tested toward formic acid oxidation, a model fuel cell reaction. Significant differences were observed between alloy and core-shell octahedra. Both particles were more active than commercially available pure platinum nanoparticles exemplifying the alloy and core-shell effect on the activity of nanoparticles. Interestingly, core-shell octahedra show higher activity than alloy octahedra and the Pt-rich composition is the most active for both alloy and core-shell octahedrons. Further studies of thinner alloy-shell core-shell nanoparticles propose a volcano-curve relationship between the lattice strain affected by alloy-shell thickness and the catalytic performance.

REFERENCES

(1) Wang, D.; Li, Y. *Advanced Materials* **2011**, *23*, 1044.

(2) Kim, J.-S.; Wieder, N. L.; Abraham, A. J.; Cargnello, M.; Fornasiero, P.; Gorte, R. J.; Vohs, J. M. *Journal of The Electrochemical Society* **2011**, *158*, B596.

(3) Joo, S. H.; Park, J. Y.; Tsung, C.-K.; Yamada, Y.; Yang, P.; Somorjai, G. A. *Nat Mater* **2009**, *8*, 126.

(4) Chen, Y.; Liang, Z.; Yang, F.; Liu, Y.; Chen, S. *The Journal of Physical Chemistry C* **2011**, *115*, 24073.

(5) Wei, W.; Li, S.; Millstone, J. E.; Banholzer, M. J.; Chen, X.; Xu, X.; Schatz, G. C.; Mirkin, C. A. *Angewandte Chemie International Edition* **2009**, *48*, 4210.

(6) Lim, B.; Jiang, M.; Camargo, P. H. C.; Cho, E. C.; Tao, J.; Lu, X.; Zhu, Y.; Xia, Y. *Science* **2009**, *324*, 1302.

(7) Tedsree, K.; Li, T.; Jones, S.; Chan, C. W. A.; Yu, K. M. K.; Bagot, P. A. J.; Marquis, E. A.; Smith, G. D. W.; Tsang, S. C. E. *Nat Nano* **2011**, *6*, 302.

(8) Strasser, P.; Koh, S.; Anniyev, T.; Greeley, J.; More, K.; Yu, C.; Liu, Z.; Kaya, S.; Nordlund, D.; Ogasawara, H.; Toney, M. F.; Nilsson, A. *Nat Chem* **2010**, *2*, 454.

(9) Bliznakov, S.; Vukmirovic, M.; Yang, L.; Sutter, E.; Adzic, R. R. *ECS Transactions* **2011**, *41*,

1055.

(10) Wang, J. X.; Inada, H.; Wu, L.; Zhu, Y.; Choi, Y.; Liu, P.; Zhou, W.-P.; Adzic, R. R. *Journal of the American Chemical Society* **2009**, *131*, 17298.

(11) Debe, M. K. *Nature* **2012**, *486*, 43.

(12) Narayanan, R.; El-Sayed, M. A. *Nano Letters* **2004**, *4*, 1343.

(13) Tian, N.; Zhou, Z.-Y.; Sun, S.-G.; Ding, Y.; Wang, Z. L. *Science* **2007**, *316*, 732.

(14) Kuai, L.; Yu, X.; Wang, S.; Sang, Y.; Geng, B. *Langmuir* **2012**, *28*, 7168.

.(15) Li, J.; Zheng, Y.; Zeng, J.; Xia, Y. *Chemistry – A European Journal* **2012**, *18*, 8150.

(16) Narayanan, R.; El-Sayed, M.A. *Nano Lett.* **2004**, 4, 1343.

(17) Habas, S.E.; Lee, H.; Radmilovic, V.; Somorjai, G.A.; Yang, P. *Nat. Mater.* **2007**, 6, 692.

(18) Wang, C.; Daimon, H.; Lee, Y.; Kim, J.; Sun, S. *J. Am. Chem. Soc.* **2007**, 129, 6974.

(19) Wang, C.; Daimon, H.; Onodera, T.; Koda, T.; Sun, S. H. *Angew. Chem., Int. Ed.* **2008**, 47, 3588.

(20) Narayanan, R.; El-Sayed, M.A. *J. Am. Chem. Soc.* **2004**, 126, 7194.

(21) Sra, A. K.; Schaak, R. E. *J. Am. Chem. Soc.* **2004**, 126, 6667.

(22) Lim, B.; Jiang, M.; Camargo, P. H. C.; Cho, E. C.; Tao, J.; Lu, X.; Zhu, Y.; Xia, Y. *Science* **2009**, 324, 1302.

(23) Macdonald, J. E.; Sadan, M. B.; Houben, L.; Popov, I.; Banin, U. *Nat. Mater.* **2010**, 9, 810.

(24) He, W.; Liu, J.; Qiao, Y.; Zou, Z.; Zhang, X.; Akins, L.D.; Yang, H. *Journal of Power Sources* **2010**, 195, 1046-1050

(25) Liu, L.; Samjeske, G.; Nagamatsu, S.; Sekizawa, O.; Nagasawa, K.; Takao, S.; Imaizumi, Y.; Yamamoto, T.; Uruga, T.; Iwasawa, Y. *J. Phys. Chem. C* **2012**, 116, 44, 23453.

(26) Cui, C.; Gan, L.; Li, H.; Yu, S.; Heggen, M.; Strasser, P. *Nano Lett* **2012**, 12, 11, 5885.

(27) Wu, Y.; Wang, D.; Niu, Z.; Chen, P.; Zhou, G.; Li, Y. *Angew. Chem. Int. Ed.* **2012**, 51, 1-6

(28) Ghosh, S.; Sahu, K.R.; Raj, R.C. *Nanotechnology* **2012**, 23, 385602

(29) Carpenter, K.M.; Moylan, E.T.; Kukreja, S.R.; Atwan, H.M.; Tessema, M.M. *J. Am. Chem. Soc.* **2012**, 134, 8535-8542

(30) Antolini, E. *Energy & Environmental Science* **2009**, *2*, 915.

(31) Zhang, L.; Lu, T.; Bao, J.; Tang, Y.; Li, C. *Electrochemistry Communications* **2006**, *8*, 1625.

(32) Mazumder, V.; Sun, S. *Journal of the American Chemical Society* **2009**, *131*, 4588.

(33) Larsen, R.; Ha, S.; Zakzeski, J.; Masel, R. I. *Journal of Power Sources* **2006**, *157*, 78.

(34) Xu, C. W.; Wang, H.; Shen, P. K.; Jiang, S. P. *Advanced Materials* **2007**, *19*, 4256.

(35) Miyake, H.; Okada, T.; Samjeske, G.; Osawa, M. *Physical Chemistry Chemical Physics* **2008**, *10*, 3662.

(36) Shao, M.-H.; Sasaki, K.; Adzic, R. R. *Journal of the American Chemical Society* **2006**, *128*, 3526.

(37) Zhou, W.; Lee, J. Y. *Electrochemistry Communications* **2007**, *9*, 1725.

(38) Suo, Y.; Hsing, I. M. *Electrochimica Acta* **2011**, *56*, 2174.

(39) Montes de Oca, M. G.; Plana, D.; Celorrio, V.; Lazaro, M. J.; Fermín, D. J. *The Journal of Physical Chemistry C* **2011**, *116*, 692.

(40) Celorrio, V.; Montes de Oca, M. G.; Plana, D.; Moliner, R.; Lázaro, M. J.; Fermín, D. J. *The Journal of Physical Chemistry C* **2012**, *116*, 6275.

(41) Lee, Y. W.; Kim, M.; Kang, S. W.; Han, S. W. *Angewandte Chemie International Edition* **2011**, *50*, 3466.

(42) Hong, J. W.; Kim, D.; Lee, Y. W.; Kim, M.; Kang, S. W.; Han, S. W. *Angewandte Chemie* **2011**, *123*, 9038.

(43) Cui, C.-H.; Yu, J.-W.; Li, H.-H.; Gao, M.-R.; Liang, H.-W.; Yu, S.-H. *ACS Nano* **2011**, *5*, 4211.

(44) Xu, J.; Wilson, A. R.; Rathmell, A. R.; Howe, J.; Chi, M.; Wiley, B. J. *ACS Nano* **2011**, *5*, 6119.

(45) Yang, C.-W.; Chanda, K.; Lin, P.-H.; Wang, Y.-N.; Liao, C.-W.; Huang, M. H. *Journal of the American Chemical Society* **2011**, *133*, 19993.

(46) Chen, M.; Kumar, D.; Yi, C.-W.; Goodman, D. W. *Science* **2005**, *310*, 291.

(47) Lee, Y. W.; Kim, M.; Kim, Z. H.; Han, S. W. *Journal of the American Chemical Society* **2009**, *131*, 17036.

(48) Lim, B.; Kobayashi, H.; Yu, T.; Wang, J.; Kim, M. J.; Li, Z.-Y.; Rycenga, M.; Xia, Y. *Journal of*

the American Chemical Society **2010**, *132*, 2506.

(49) Ding, Y.; Fan, F.; Tian, Z.; Wang, Z. L. *Journal of the American Chemical Society* **2010**, *132*, 12480.

(50) Yang, J; Yang, J; Ying, Y. J. *ACS Nano* Articles ASAP.

(51) Zhang, G.; Wu, J.; Xu, B. *J. Phys. Chem. C* **2012**, 116, 20839-20847

(52) Kuai, L.; Yu, X.; Wang, S.; Sang, Y.; Geng, B. *Langmuir* **2012**, 28, 7168-7173

(53) Stamenkovic, V. R.; Fowler, B.; Mun, B. S.; Wang, G.; Ross, P. N.; Lucas, C. A.; Marković, N. M. *Science* **2007**, *315*, 493.

CHAPTER 2

Experimental Procedures

2.1 Chemicals

In a typical co-reduction synthesis, metal precursors are reduced by reducing agent in aqueous system in which surfactants dissolve. Cetyltrimethylammonium bromide (CTAB, 98 %, CALBIOCHEM) and cetyltrimethylammonium chloride (CTAC, 95 %, TGI) were used as surfactants. These ionic surfactants were known to be efficient to make cleaner surface nanoparticles. Palladium (Ⅱ) chloride ($PdCl_2$, 99 %, Sigma Aldrich), potassium tetrachloroplatinate (Ⅱ) (K_2PtCl_4, ≧99 %, Sigma Aldrich) and gold (Ⅲ) chloride hydrate ($HAuCl_4$, 99.99%, Sigma Aldrich) were used to prepare 0.01M metal precursors. Sodium citrate tribasic dehydrate ($C_6H_5Na_3O_7 \cdot 2H_2O$, Sigma Aldrich, 99.5 %) was used as a reducing agent. All the chemicals were used without further purification. Ultrapure distilled and deionized water (18.2 MΩ) was used for all solution preparations. Ultrapure Argon (Ar, Airgas) and carbon monoxide (CO, Airgas) were used during the synthesis.

2.2 Synthetic Procedure

2.2.1 Synthesis of PdPt Alloy Octahedral Nanoparticles

Octahedral PdPt alloy nanoparticles were prepared by one-pot hydrothermal method in 30 mL aqueous solution. A pressure vessel containing 28.98 mL of deionized

water, 102.45 mg CTAB and 18 mg CTAC was sonicated until it became clear, indicating the surfactants were completely dissolved. Then, 0.375 mL of 0.01 M H_2PdCl_4 solution and 0.375 mL of 0.01 M K_2PtCl_4 solution were added. After being bubbled by argon for half an hour, 0.142 mL of 0.1 M sodium citrate solution was added into the salmon-pink color cloudy solution. The pressure vessel was then placed and heated at 110 ℃ for 22 hours in the oven. The resulting brown color transparent solution was cooled down to room temperature. The products were collected by centrifugation at 12,000 rpm three times and then redispersed in deionized water.

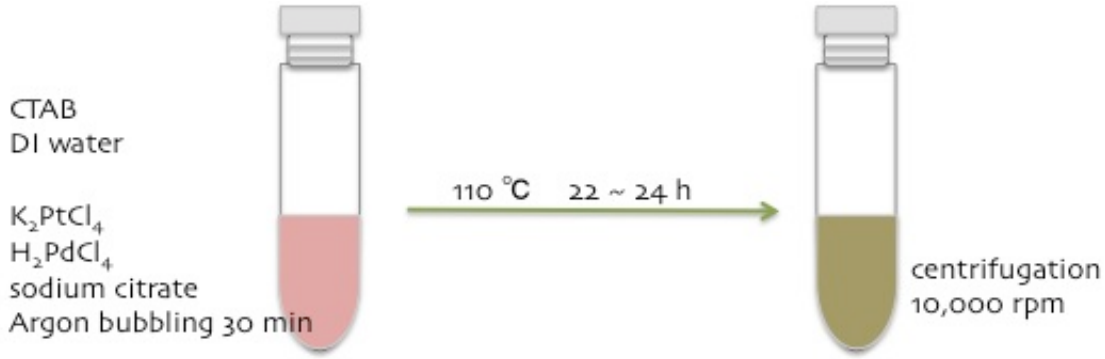

Scheme 2.1 Schematic illustration of the procedure used for preparing PdPt alloy octahedral nanoparticles.

2.2.2 Preparation of Gold Seeds

Sub-10 nm spherical gold seeds were prepared by a simple one-pot hydrothermal method in aqueous system. First, 0.27 g CTAB was dissolved in 48.51 mL of deionized water. Then, 1.25 mL of 0.01 M $HAuCl_4$ and 0.237 mL of 0.1 M sodium citrate were added into the clear transparent solution, followed by bubbling carbon monoxide for half an hour. The right-orange solution in a pressure vessel was heated at 110 ℃ for 22

hours and the red-violet color solution was obtained.

2.2.3 Synthesis of Au@PdPt Core-Shell Octahedral Nanoparticles

In the typical synthesis of octahedral Au@PdPt core-shell nanoparticles, a pressure vessel containing 25.98 mL of deionized water, 102.45 mg CTAB and 18 mg CTAC was sonicated until it became clear transparent. Once these surfactants were dissolved, 3 mL of Au-seed solution was added, followed by the further addition of 0.375 mL of 0.01 M H_2PdCl_4 solution and 0.375 mL of 0.01 M K_2PtCl_4 solution. After being bubbled by argon for half an hour, 0.142 mL of 0.1M sodium citrate solution was added into the pale-violet color cloudy solution. The vessel was then heated at 110 ℃ for 22 hours in the oven. The resulting brown color transparent solution in a pressure vessel was cooled down to room temperature. The products were collected by centrifugation at 12,000 rpm three times and then redispersed in deionized water.

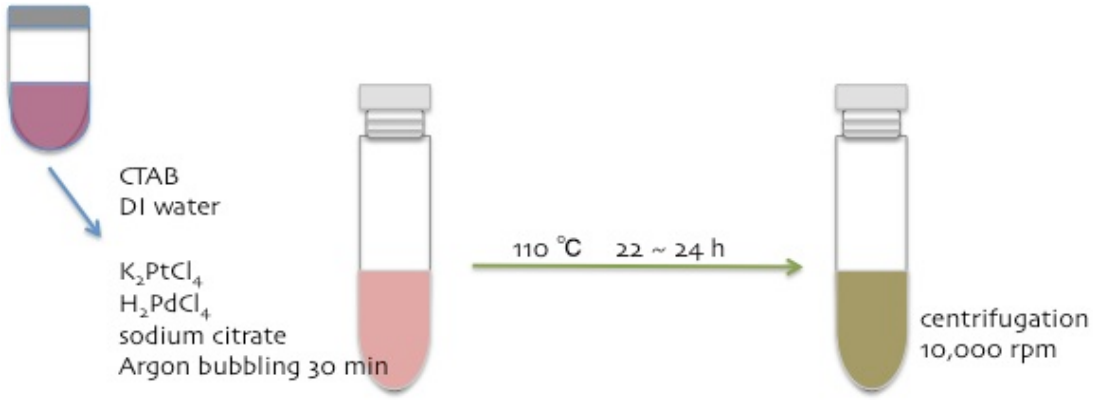

Scheme 2.2 Schematic illustration of the procedure used to synthesize Au@PdPt core-shell octahedral nanoparticles.

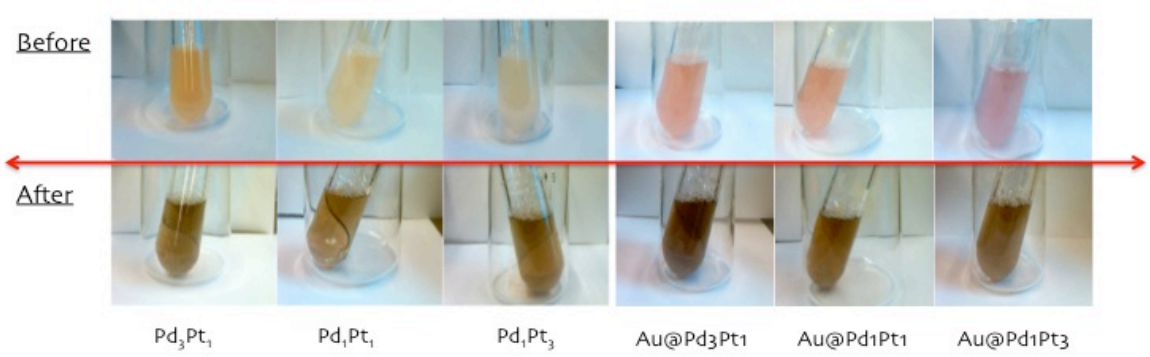

Figure 2.1 Picture of the growth solution color changes before and after the heating.

2.3 Sample Preparation for Characterization

2.3.1 Sample Preparation for TEM (Transmission Electron Microscope) and EDS (Electron Diffraction Spectroscopy)

Samples were prepared for TEM and EDX spectroscopy by washing several times with deionized water and placing 2.5 μL droplets of particle solutions on carbon-coated copper grids (TED PELLA, INC. Lacey Carbon Type-A), which were then allowed to dry open to the air.

2.3.2 Sample Preparation for ICP-OES (Inductively Coupled Plasma Optical Emission Spectrometry)

For ICP-OES measurement, 300 μ L of concentrated hydrochloric acid and 100

μL of concentrated nitric acid were added into particle solution which was washed several times with deionized water and then concentrated to 0.1 mL solution. The color of particle solution changed from brown to pale yellow, indicating all the metal nanoparticles are oxidized. Then, particle solution was diluted to 10 mL.

2.3.3 Sample Preparation for Powder-XRD (X-ray Diffraction Spectroscopy)

Samples for XRD were prepared by placing 20 μL aliquots of concentrated nanoparticle solution with in portions of 5 μL on a silicon wafer and allowing them to dry in air.

2.4 Electrochemical Measurement Procedure

2.4.1 Blank Scan

A three-electrode cell system was utilized to measure the electrochemical properties. A glassy carbon electrode (CH Instruments) was used as the working electrode and polished with 0.3 micron micropolish powder (CH Instruments) several times. A saturated calomel electrode (CH Instruments) and a platinum wire were used as a reference and counter electrode, respectively. First, a blank scan was performed in N_2-saturated fresh 0.5 M H_2SO_4 solution with the potential from -0.2 V to 1.0 V in order to clean the surface of the working electrode. In a typical measurement, the blank scan was continued through for around 10 cycles. Then, the working electrode was taken out

from the 0.5 M H_2SO_4 solution and placed aside until it dried. Next, 5 μ L of deionized dispersion of purified nanoparticles was deposited on a glassy carbon electrode. After the working electrode was dried, the blank scan was carried out to clean the surface of sample-deposited working electrode with the same scanning condition for around 200 cycles.

2.4.2 Formic Acid Oxidation

For the electro-oxidation of formic acid, the cyclic voltammogram was recorded at a sweep rate of 100 mV/s in N_2-saturated fresh 1 M H_2SO_4 and 1 M formic acid mixed solution with the potential range from -0.2 V to 1.0 V for around 80 cycles. The current is normalized by the electrochemically active surface area (ECSA) of catalysts in the electrode, which was estimated from the integrated reduction charge of surface palladium oxide by assuming a charge of 0.42 mC/cm^2 for the reduction of palladium oxide monolayer.

2.4.3 CO Stripping

For the CO stripping voltammetry measurements, CO gas was bubbled for 30 minutes through 0.1 M $HClO_4$ solution in which the sample-deposited working electrode was immersed. The electrode was moved to a fresh N_2-saturated 0.1 M $HClO_4$ solution and the CO stripping voltammetry was recorded at a sweep rate of 10 mV/s with the potential range from -0.2 V to 1.0 V. This procedure was repeated several times until the peak position and the peak height get stable. The electrochemically active surface area (ECSA) of the electrode was determined by measuring the charge in the CO-stripping

peak of the voltammogram.

2.5 Instrumentation

The growth solution was heated in an oven, using a Thermo SCIENTIFIC LINDBERG BLUE M. The particles were collected by using a Thermo SCIENTIFIC SORVALL LEGEND X1R Centrifuge and an eppendorf Centrifuge 5424. Transmission electron microscopy (TEM) including high-resolution transmission electron microscope (HRTEM) and energy-dispersive X-ray spectroscopy (EDS) studies were performed on a JOEL JEM 2010F electron microscope operating at 200 kV. Powder X-ray diffraction (XRD) patterns were recorded using a Bruker AXS diffractometer with CuKα radiation. (Wavelength: 1.54060 Å) Inductively coupled plasma optical emission spectrometry was performed using a PerkinElmer Inc. Optima 2100 DV. Electrochemical measurements were carried out with a potentiostat system, BioLogic VSP.

CHAPTER 3

Characterization and Analysis

3.1 Size and Shape Characterization: TEM and HRTEM

3.1.1 Gold Seeds

The small, monodisperse 8nm gold seeds (Figure 3.1-a) were synthesized through a hydrothermal method. Since ionic surfactant, cetyltrimethylammonium bromide, was used in the synthesis, by washing the sample solution several times the resulting nanoparticles have almost no significant coverage caused by surfactant. Carbon monoxide was bubbled into the solution before heating. The carbon monoxide dissolved into the solution was found to greatly influence seed size and shape. With bubbling carbon monoxide during the seed solution synthesis, uniform spherical gold nanoparticles were obtained. Without bubbling carbon monoxide during the seed solution synthesis, larger irregularly shaped particles unsuited for coating resulted. (Figure 3.1-b)

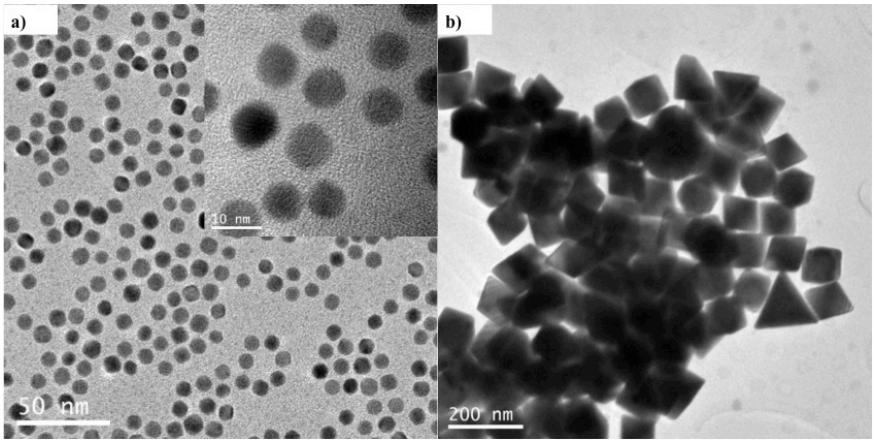

Figure 3.1 TEM images of as-synthesized gold seeds a) with CO bubbling and b) without CO bubbling.

3.1.2 PdPt Alloy Octahedral Nanoparticles

To evaluate the size and shape of PdPt alloy particles, TEM images were taken. (Figure 3.2 a-c) The alloy nanoparticles were found to be monodispersed with a narrow particle size distribution. The average particle size is 10.3 nm for Pd_3Pt_1, 9.1 nm for Pd_1Pt_1 and 8.1 nm for Pd_1Pt_3 nanoparticles. The majority of the alloy particles appeared in uniform with well-defined octahedral shape. Figure 3.2 d-f shows high-resolution TEM (HRTEM) images for alloy nanoparticles. Their lattice fringe orientations reveal that they were single crystalline. The corresponding d-spacing for (111) crystal facet is calculated as 0.231 nm for Pd_3Pt_1, 0.229 nm for Pd_1Pt_1 and 0.231 nm for Pd_1Pt_3 alloy octahedral nanoparticles.

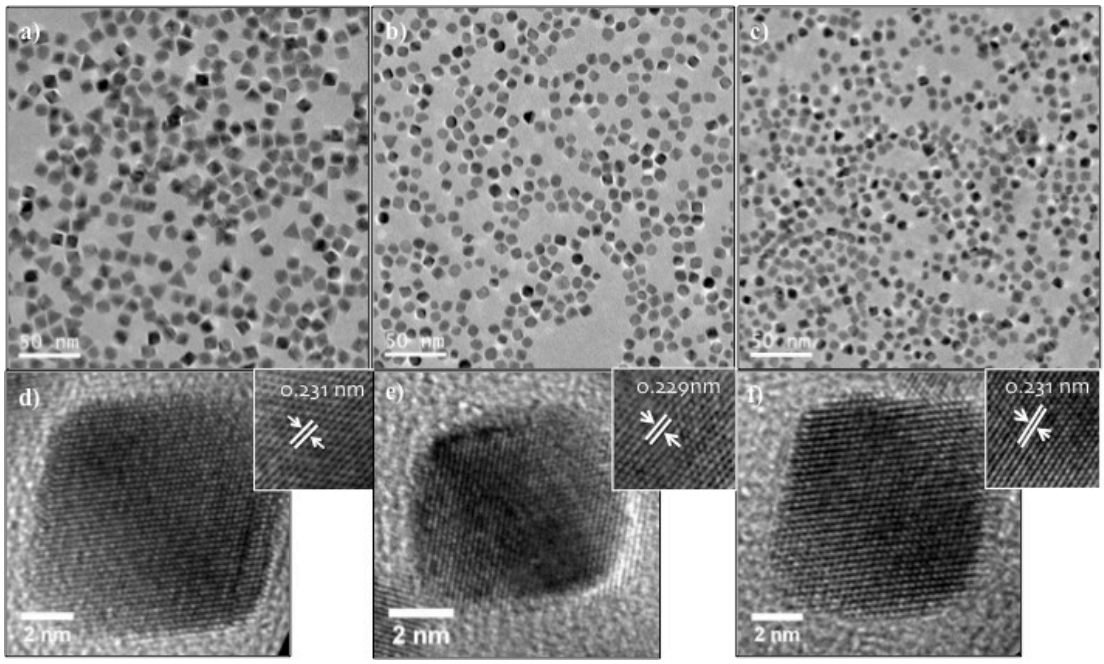

Figure 3.2 TEM and the corresponding HRTEM images for a, d) Pd_3Pt_1 b, e) Pd_1Pt_1 c, f) Pd_1Pt_3 alloy octahedral nanoparticles.

3.1.3 Au@PdPt Core-shell Octahedral Nanoparticles

Figure 3.3 shows the representative TEM images for Au@PdPt core-shell particles. The particles have octahedral shape. The average core-shell particle size is found to be 16.5 nm for $Au@Pd_3Pt_1$, 15.7 nm for $Au@Pd_1Pt_1$ and 15.9 nm for $Au@Pd_1Pt_3$ nanoparticles. The lattice orientations in the HRTEM confirm that they are single crystalline. Based on the HRTEM (Figure 3.3 d-f), the calculated d-space values for (111) crystal facet are 0.235 nm (Au core)/ 0.232 nm (PdPt alloy-shell) for $Au@Pd_3Pt_1$, 0.235 nm (Au core)/ 0.228 nm (PdPt alloy-shell) for $Au@Pd_1Pt_1$, and 0.236 nm (Au core)/ 0.233 nm (PdPt alloy-shell) for $Au@Pd_1Pt_3$ core-shell octahedral nanoparticles.

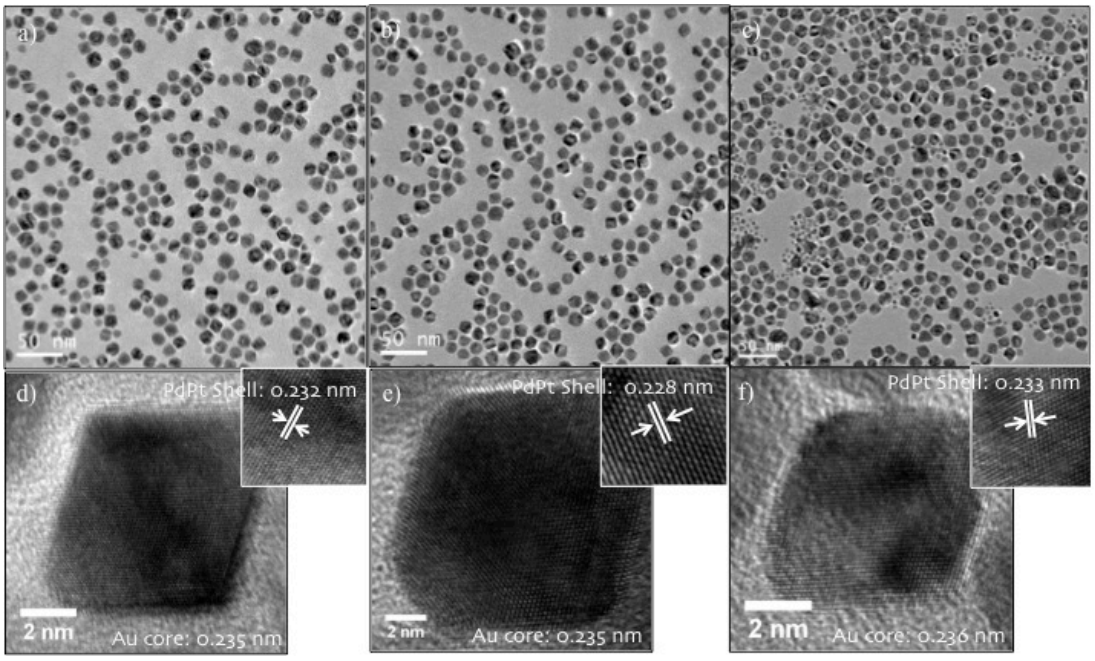

Figure 3.3 TEM and the corresponding HRTEM images for a, d) $Au@Pd_3Pt_1$ b, e) $Au@Pd_1Pt_1$ c, f) $Au@Pd_1Pt_3$ core-shell octahedral nanoparticles.

3.2 Elemental Analysis: EDS and ICP-OES

3.2.1 PdPt Alloy Octahedral Nanoparticles

To better describe the resulting particles, energy dispersive X-ray spectroscopy (EDS) and inductively coupled plasma optical emission spectrometry (ICP-OES) were used to verify the overall atomic percentage of Pt and Pd. (Table 3.1) The elemental analysis results confirm that PdPt alloy nanoparticles were indeed composed of platinum and palladium. Although the alloy compositions were supposed to be Pd_3Pt_1, Pd_1Pt_1 and Pd_1Pt_3, the EDS and ICP-OES data verified that Pd_1Pt_1 alloy particles have slightly more palladium than platinum and Pd_1Pt_3 alloy particles have much less platinum than expected by the precursor ratios.

Expected	EDS	ICP-OES
Pd_3Pt_1	$Pd_{79}Pt_{21}$ (Pd_4Pt_1)	$Pd_{3.195}Pt_1$ ($Pd_{3.2}Pt_1$)
Pd_1Pt_1	$Pd_{57}Pt_{43}$ ($Pd_{1.5}Pt_1$)	$Pd_{1.952}Pt_1$ (Pd_2Pt_1)
Pd_1Pt_3	$Pd_{39}Pt_{61}$ ($Pd_1Pt_{1.5}$)	$Pd_1Pt_{1.608}$ ($Pd_1Pt_{1.6}$)

Table 3.1 EDS and ICP-OES elemental analysis results for PdPt alloy octahedral nanoparticles with three different compositions.

3.2.1 Au@PdPt Core-shell Octahedral Nanoparticles

Table 3.2 shows the EDS and ICP-OES elemental analysis results for Au@PdPt core-shell octahedral nanoparticles. The PdPt alloy-shell compositions of Au@PdPt core-shell particles were close to those of pure PdPt alloy nanoparticles. Since the PdPt alloy shell is relatively thick (about 5 nm), core to shell ratio of the Au@PdPt core-shell

nanoparticles were difficult to determine accurately using standard TEM technique. The gold core to PdPt alloy-shell ratio determined by ICP-OES was 1:3.328, 1:2.838, and 1:2.582 for Au@Pd_3Pt_1, Au@Pd_1Pt_1, and Au@Pd_1Pt_3 respectively, while the expected core to alloy-shell ratio is set as 1:10.

Expected	EDS	ICP-OES
Pd_3Pt_1	$Pd_{80}Pt_{20}$ (Pd_4Pt_1)	$Pd_{2.739}Pt_1$ ($Pd_{2.7}Pt_1$)
Pd_1Pt_1	$Pd_{60}Pt_{40}$ ($Pd_{1.5}Pt_1$)	$Pd_{1.160}Pt_1$ ($Pd_{1.2}Pt_1$)
Pd_1Pt_3	$Pd_{37}Pt_{63}$ ($Pd_1Pt_{1.5}$)	$Pd_1Pt_{1.713}$ ($Pd_1Pt_{1.7}$)

Table 3.2 EDS and ICP-OES elemental analysis results for PdPt alloy-shell of Au@PdPt core-shell octahedral nanoparticles with three different compositions.

3.3 Crystallographic Analysis: Powder-XRD

3.3.1 XRD profiles of PdPt Alloy Octahedral Nanoparticles

PdPt alloy nanoparticles were characterized by powder X-ray diffraction (XRD) as shown in Figure 3.4. The XRD patterns obtained from both PdPt alloy nanoparticles could be indexed to (111), (200), (220) and (311) diffraction peaks, which correspond to a face-centered-cubic (fcc) structure. The peak angle values for each crystal facet are listed in Table 3.3. A single peak for each crystal facet verifies that the particles are PdPt alloyed particles. The lattice parameters were calculated based on the Bragg's law ($\lambda = 2d\sin\Theta$) and listed in Table 3.4 for PdPt alloy particles.

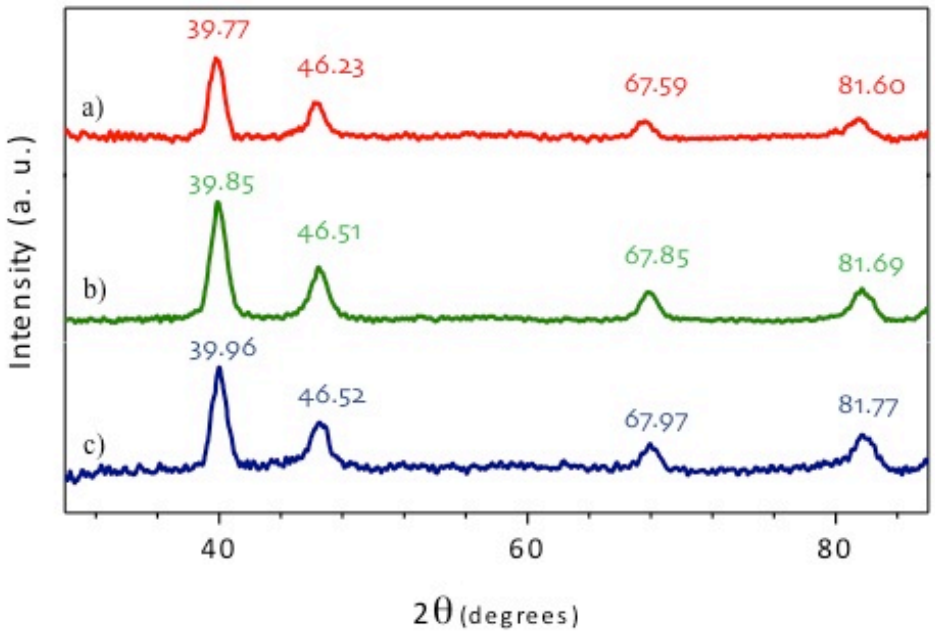

Figure 3.4 XRD patterns for a) Pd_1Pt_3, b) Pd_1Pt_1 and c) Pd_3Pt_1 alloy nanoparticles.

	111	200	220	311
Pd_1Pt_3	39.77	46.23	67.59	81.60
Pd_1Pt_1	39.85	46.51	67.85	81.69
Pd_3Pt_1	39.96	46.52	67.97	81.77

Table 3.3 XRD 2Θ values for each crystal facet of PdPt alloy octahedral nanoparticles.

d (Å)	111	200	220	311
Pd_1Pt_3	2.264	1.961	1.384	1.178
Pd_1Pt_1	2.260	1.950	1.380	1.177
Pd_3Pt_1	2.253	1.950	1.378	1.176

Table 3.4 The d-space length for PdPt alloy nanoparticles for each crystal facet.

3.3.2 XRD profiles of Au@PdPt Core-shell Octahedral Nanoparticles

Figure 3.5 reports the XRD patterns for the Au@PdPt core-shell octahedral nanoparticles including gold seeds and Pd_1Pt_1 alloy particles. A typical fcc crystal phase can be found. The peak angle values for each crystal facet are listed in Table 3.5. The d-space values were calculated based on the Bragg's law ($\lambda = 2d\sin\Theta$) and listed in Table 3.6. It is obviously noted that there are two distinctive peaks for each crystal facet, indicating the particles are core-shell particles. The XRD peak profile and the obtained d-space values confirmed that the first peak can be assigned to gold core and the second peak can be assigned to PdPt alloy-shell for each crystal facet.

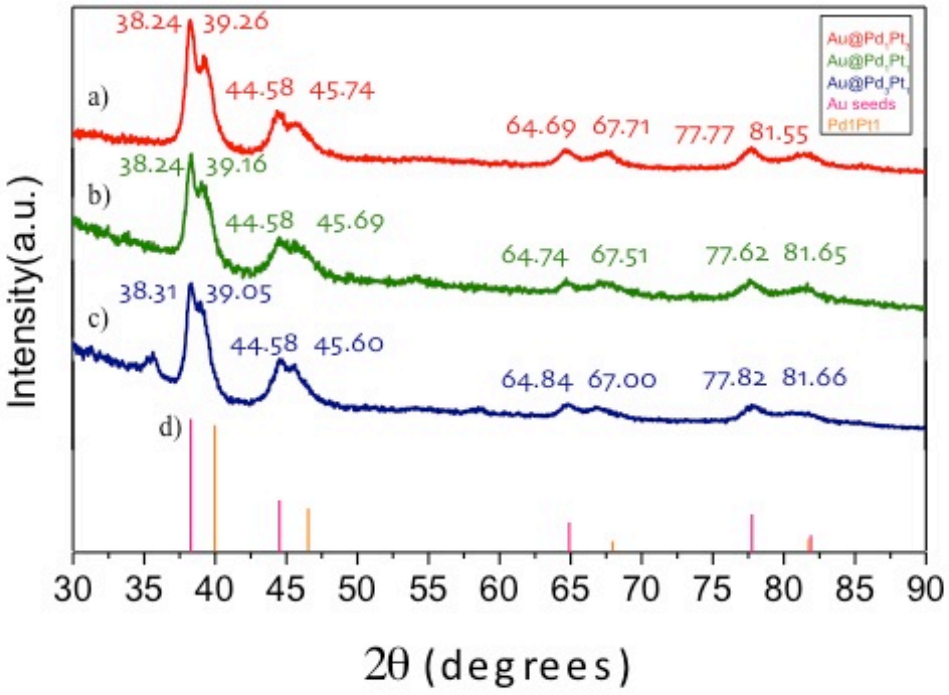

Figure 3.5 XRD patterns for a) $Au@Pd_1Pt_3$, b) $Au@Pd_1Pt_1$, c) $Au@Pd_1Pt_3$ core-shell octahedral nanoparticles and d) gold seeds (Pink line) and Pd_1Pt_1 alloy(Orange line).

	111	200	220	311
Au seeds	38.26	44.56	64.76	77.79
$Au@Pd_1Pt_3$	38.24	44.58	64.69	77.77
	39.26	45.74	67.71	81.55
$Au@Pd_1Pt_1$	38.24	44.58	64.74	77.62
	39.16	45.69	67.51	81.65
$Au@Pd_3Pt_1$	38.31	44.58	64.84	77.82
	39.05	45.60	67.06	81.66

Table 3.5 XRD 2Θ values for each crystal facet of gold seeds and Au@PdPt core-shell nanoparticles.

	111	200	220	311
Au seeds	2.350	2.031	1.438	1.226
$Au@Pd_1Pt_3$	2.352	2.031	1.440	1.227
	2.293	1.982	1.383	1.179
$Au@Pd_1Pt_1$	2.352	2.031	1.439	1.229
	2.299	1.984	1.386	1.178
$Au@Pd_3Pt_1$	2.348	2.031	1.437	1.226
	2.305	1.988	1.395	1.178

Table 3.6 The d-space values for gold seed and Au@PdPt core-shell nanoparticles.

3.4 XRD (220) Pattern Analysis

3.4.1 PdPt Alloy Octahedral Nanoparticles

Figure 3.6 shows the XRD (220) peak pattern analysis for all three compositions of PdPt alloy nanoparticles. All the (220) peaks are located in between the normal Pd (220) peak at 68.18 and Pt (220) peak at 67.5, indicating they are alloy crystals. Interestingly, the sequence of these three peaks is different from what it should be, but have inversed sequence in compositional variation.

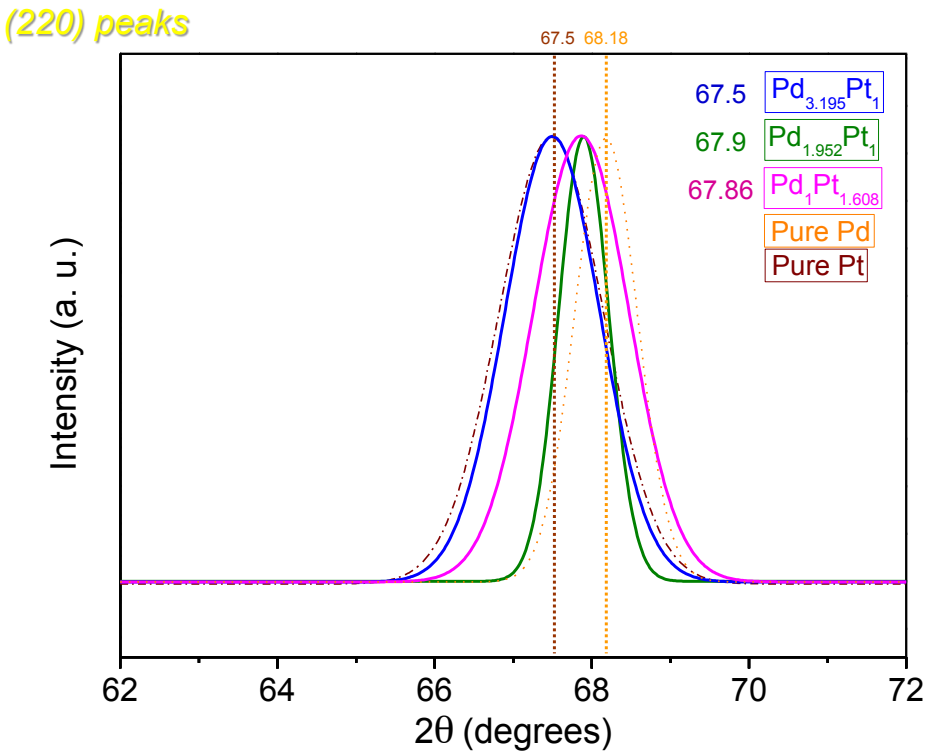

Figure 3.6 XRD (220) patterns of PdPt alloy particles with three different compositions.

3.4.2 Au@PdPt Core-shell Octahedral Nanoparticles

As with the PdPt alloy nanoparticles, the XRD (220) peak patterns were analyzed for all the core-shell nanoparticles. Figure 3.7 shows the XRD (220) patterns of Au@PdPt core-shell octahedral nanoparticles with three different alloy-shell compositions. The elemental ratios of alloy-shell were validated by ICP-OES. Noticeably, all the PdPt alloy-shell peaks were not in between normal Pt and Pd peaks, but significantly shifted further to lower 2Θ values. These peak shifts could be attributed to the lattice expansion due to the indirect relationship between peak angle and d-space. In addition, slight peak shifts to higher 2Θ were observed for all the gold-core peaks,

indicating the lattice contraction on the gold core. It is interesting to note that the sequence of the PdPt alloy-shell compositions is again in inversed order.

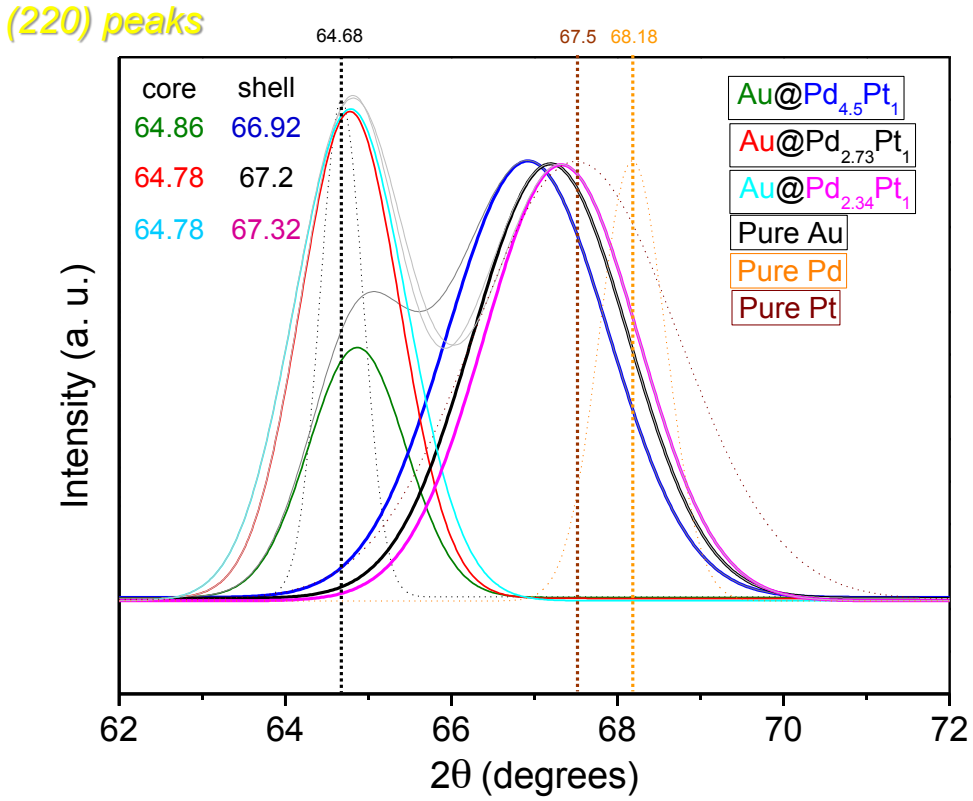

Figure 3.7 XRD (220) patterns of Au@PdPt core-shell nanoparticles with three different alloy-shell compositions.

3.5 PdPt Alloy Octahedral Nanoparticles Formation Mechanism

3.5.1 Reducing Agent: Sodium Citrate and Ascorbic Acid

To obtain further insight in the formation mechanism of PdPt alloy octahedral nanoparticle, the influence of reducing agent strength was studied first. In a typical synthesis of alloy nanoparticles, a mild reducing agent, sodium citrate, is used to reduce

the metal precursors. As Figure 3.8 shows, uniform and monodispersed octahedral PdPt alloy nanoparticles were obtained when sodium citrate is used as a reducing agent. When stronger reducing agent, ascorbic acid, is mixed with sodium citrate and used as a reducing agent, the octahedral structure was no longer obtained. As the amount of ascorbic acid increases over sodium citrate, the resulting particles become a dendritic structure, which can be attributed to the separated reduction kinetics of Pt and Pd metal precursors caused by ascorbic acid because Pt is easier to be reduced than Pd. A Pt core would be formed first and Pd is grown on the Pt core, resulting in a dendritic structure. Employing sodium citrate as a reducing agent is important to decrease the reduction rate and lead to co-reduction of Pt and Pd metal precursors, thereby promoting a well-alloyed PdPt particle formation.

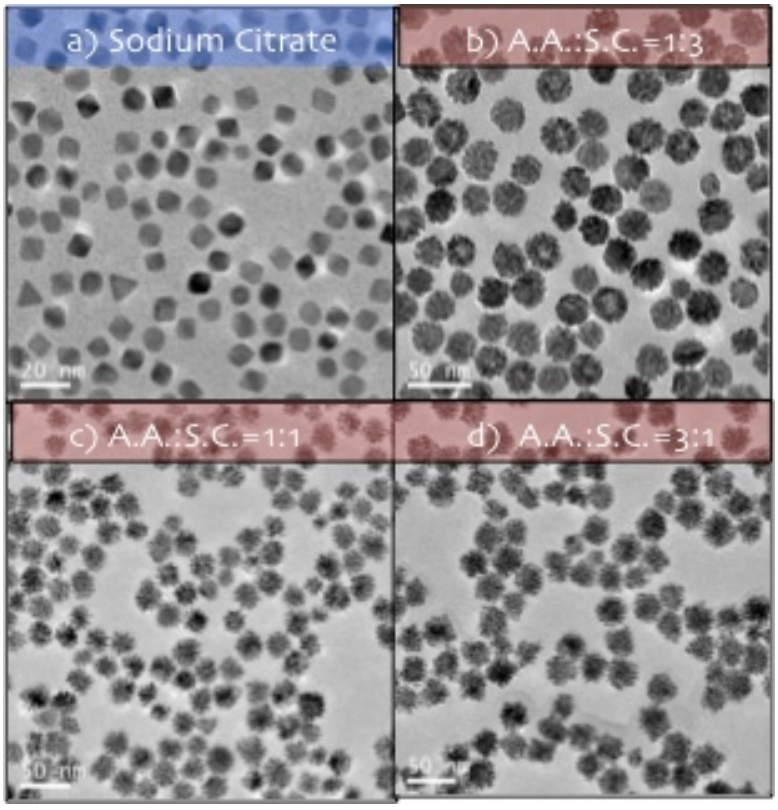

Figure 3.8 Pd_1Pt_1 alloy nanoparticles with a) sodium citrate and the mixture of ascorbic

acid and sodium citrate with the ratio of b) 1:3, c) 1:1 and d) 3:1.

3.5.2 Gas Type introduced during synthesis: Argon, Air and Oxygen

In order to investigate the role of the introduced gas type, argon, during the synthesis, air and oxygen were used in a synthesis. Figure 3.9 demonstrates the difference among the gas types utilized during the alloy particles synthesis. With argon, the smallest octahedron can be obtained and with oxygen the particle size grows to 14 nm and the octahedrons becomes sharper. The synthesis with air produced octahedrons in between those with argon and oxygen. Argon serves to remove oxygen from the growth solution and less oxygen produces smaller and uniform nanoparticles.

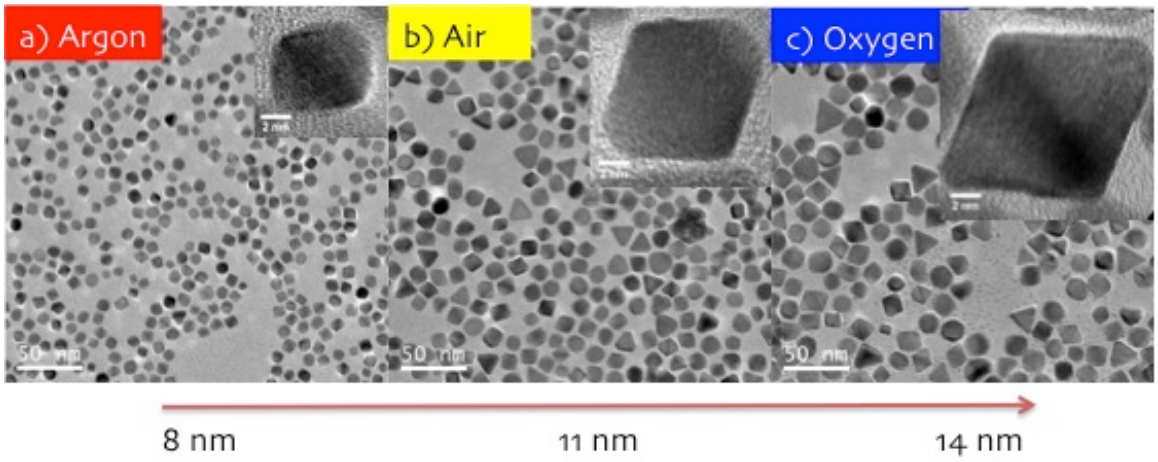

Figure 3.9 Pd_1Pt_1 alloy nanoparticles with introducing a) argon, b) air and c) oxygen gases during the synthesis.

3.5.3 Sodium Citrate Amount and Gas type

Since the particle size depends on the introduced gas type during the synthesis and the morphology of the particles seems to be induced from the reducing agent type, the effect combining these two factors were examined. (Figure 3.10) When argon was used during the synthesis and at the same time the amount of sodium citrate was changed, less reducing agent resulted in less defined octahedral structure, but the particle size was not affected with the amount of reducing agent. When oxygen was introduced in the synthesis, less defined and much bigger alloy particles were obtained depending on the amount of the reducing agent. Both argon and the amount of sodium citrate play an important role to achieve small and well-defined octahedrons.

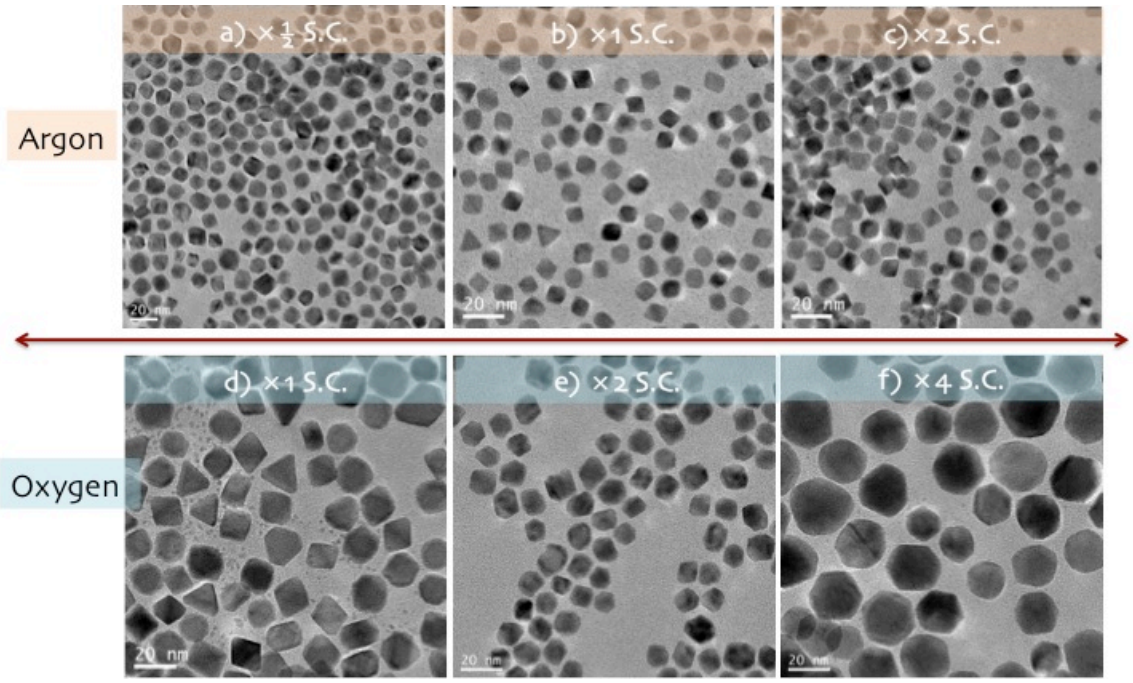

Figure 3.10 TEM images for Pd_1Pt_1 alloy nanoparticles with either argon and a) half, b) usual, c) twice amount of sodium citrate, or oxygen and d) usual, e) twice, and f) four times more amount of sodium citrate.

3.5.4 Particle Formation Scheme

Based on the above experimental results, Scheme 3.1 demonstrates the PdPt alloy particle formation mechanism. Both platinum and palladium metal precursors are reduced almost simultaneously by mild reducing agent and nucleation occurs. Reduction process continues and the nucleus grows. At the growth stage, the low coordination number atoms on the nucleus are more active to be oxidized by oxygen in the solution and back to the ion state, and again these ions are reduced by the reducing agent. Involving such etching process, smooth and stable surface structure is formed, which causes the octahedral structure that is enclosed by thermodynamically most stable 111 facets.

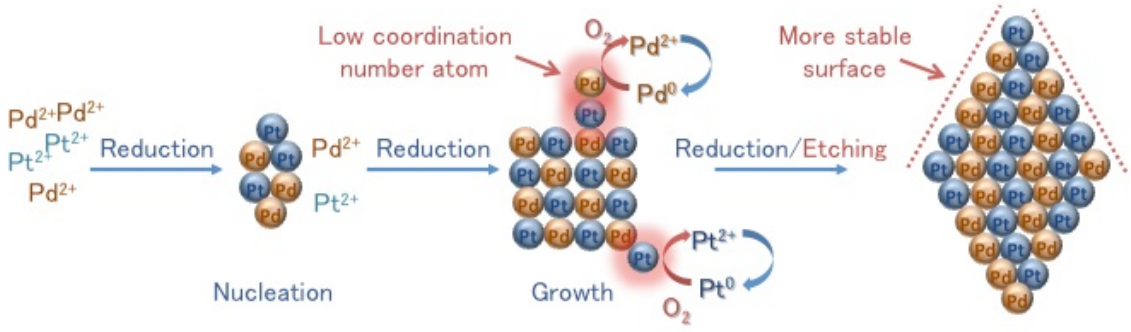

Scheme 3.1 Schematic illustration of octahedral PdPt alloy nanoparticle growth mechanism.

Scheme 3.2 explains what would happen to the particle if the stronger reducing

agent is used or less and more oxygen is present in the growth solution. The stronger reducing agent enhances the separated Pd and Pt reduction process causing the dendritic structure. When argon is introduced, most of the oxygen present in the solution is removed, which allow smaller nucleus to grow and resulted in small and smooth structure. If there is more oxygen present in the solution, some of the reducing agent is directly consumed and fewer nuclei would be produced. Simultaneous redox reaction is also enhanced, causing the larger and smooth structure formation.

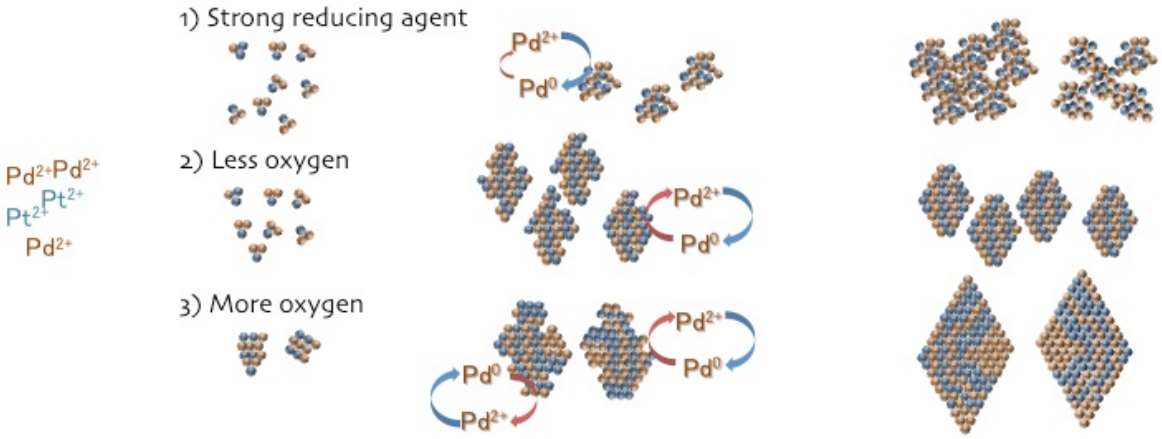

Scheme 3.2 Schematic illustration of octahedral PdPt alloy nanoparticle formation mechanism: 1) with strong reducing agent 2) less oxygen in the system (argon is introduced) 3) more oxygen in the system (oxygen is introduced).

CHAPTER 4

Electrochemical Measurements

4.1 Formic Acid Oxidation Reaction

In direct formic acid fuel cells (DFAFC), formic acid is oxidized at the anode and oxygen is reduced at the cathode. This DFAFC can be suitable for applications involving portable electronic devices. There are several advantages in DFAFCs. First, the oxidation of formic acid possesses relatively faster kinetics than other common alcohols such as methanol and ethanol. Secondly, there is less crossover. Lastly, transportation of liquid formic acid is much safer than hydrogen gas. It is widely accepted that there are two different reaction pathways for formic acid oxidation: direct pathway[1] and indirect pathway[2]. (Figure 4.1) In direct pathway, formic acid is directly oxidized into carbon dioxide and Palladium prefers to proceed via the direct pathway. Indirect pathway involves the formation of a poisoning species, carbon monoxide and Platinum prefers the indirect pathway. Palladium is active toward formic acid oxidation because it does not produce poisoning intermediates, but it is deactivated rapidly. Platinum is less active than palladium, but much more stable. It is expected that alloying platinum and palladium can make the best of both metals and enhance the catalytic activity.

---

1 Suo, Y.; Hsing, M.I. *Electrochemica Acta* **2009**, 55, 210.
2 Nazar, F. L et.al., *Nat. Chem* **2010**, 2, 286.

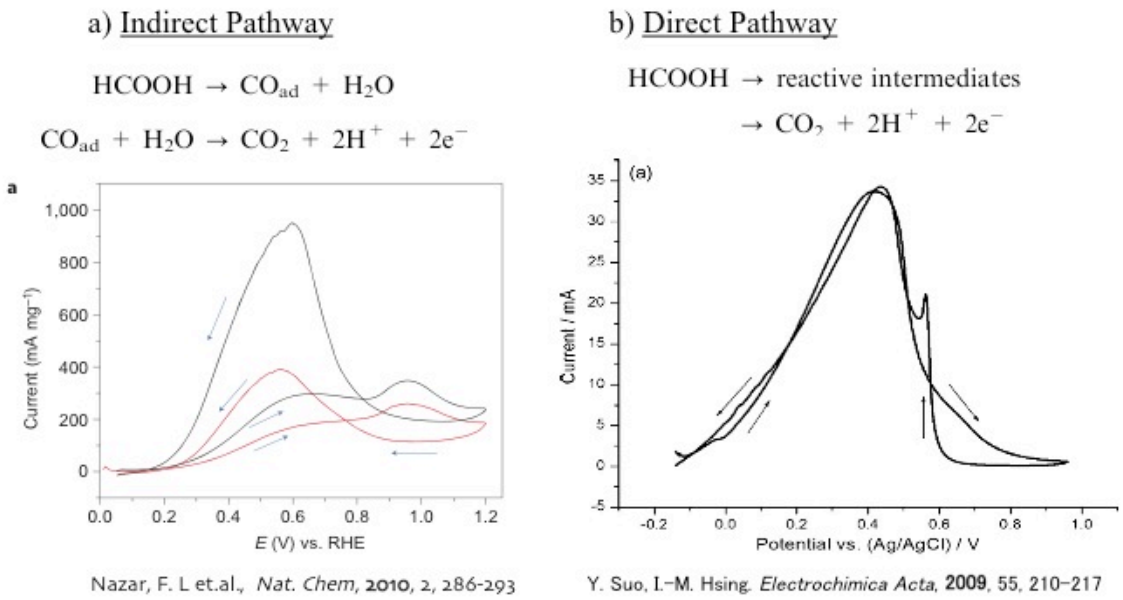

Figure 4.1 The oxidation of formic acid in a) indirect pathway and b) direct pathway.

4.2 Electrochemical Measurements

4.2.1 Blank Scan

The surface of the working electrode was cleaned with blank scans. (Figure 4.2) The typical blank scan looks elliptical in shape. If it is closer to a rectangular shape, then the electrode is clean enough.

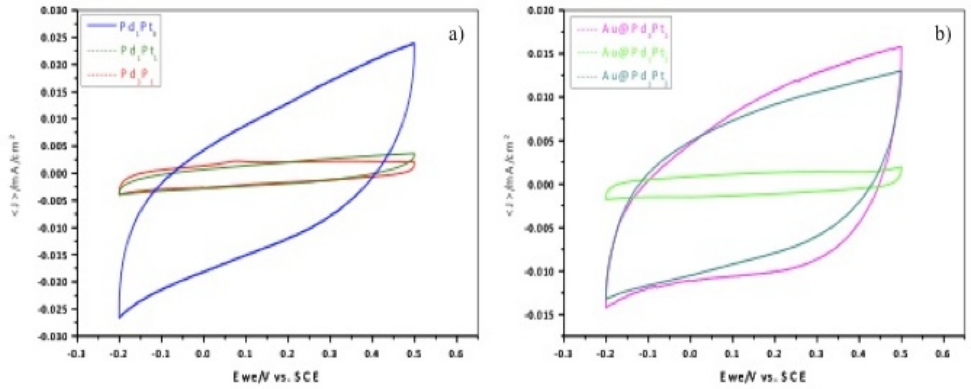

Figure 4.2 Blank scan of electrode used in the measurements for a) PdPt alloy b) Au@PdPt core-shell octahedral nanoparticles.

After confirming the surface of the electrode is clean, the electrode was taken out from the cell and dried. Then, 5 μL of the sample solution was dropped on the electrode and dried. As shown in Figure 4.3, the blank scan of the working electrode with catalyst was carried out for all the PdPt alloy and Au@PdPt core-shell nanoparticles in the same 0.5 M H_2SO_4 solution. Usually, the hydrogen absorption and desorption peaks appear on the left side and the oxygen reduction peak can be seen on the right side of the cyclic voltammogram. The more the stronger the peak, the cleaner the electrode surface is.

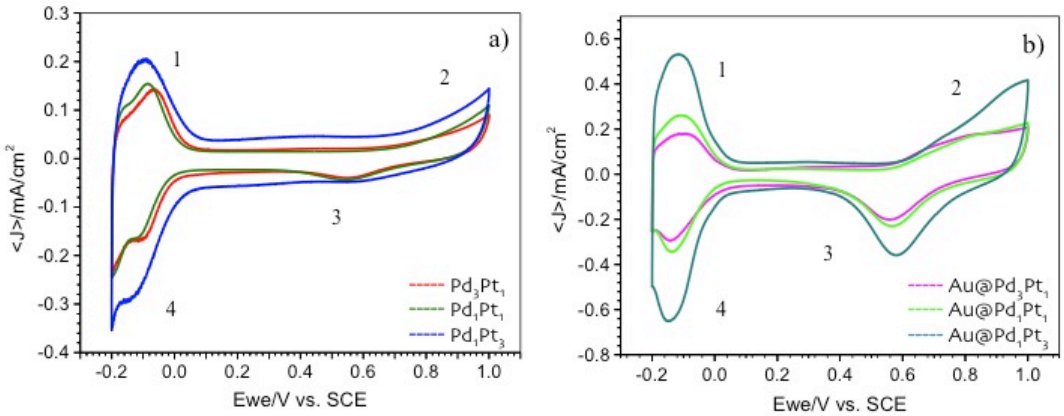

1. Hydrogen desorption peak
2. Anodic peak
3. Oxygen reduction peak
4. Hydrogen adsorption peak

Figure 4.3 Blank scan of electrode with a) PdPt alloy b) Au@PdPt core-shell octahedral nanoparticles with three different alloy compositions.

4.2.2 CO stripping

In order to determine the surface area of the electrocatalyst, a CO stripping scan was measured. Table 4.1 summarizes the CO stripping peak positions and the corresponding surface areas for all the alloy and core-shell nanoparticles. Depending on how easily carbon monoxide absorbed and oxidized on the metal catalyst, the peak potential differs. (Scheme 4.1) Once the surface area of the catalyst was obtained, the current density for the targeted fuel cell reaction can be calculated by normalizing this surface area.

$$CO_{ads} + OH_{ads} \rightarrow CO_2 + H^+ + e^- + 2*$$

Scheme 4.1 The chemical equation for CO oxidation

Electrocatalyst	Peak Position (e/V)	Surface Area (cm^2)
Alloy: Pd_3Pt_1	0.589	0.295
Alloy: Pd_1Pt_1	0.518	1.095
Alloy: Pd_1Pt_3	0.536	0.204
Core-Shell: Au@Pd_3Pt_1	0.589	0.832
Core-Shell: Au@Pd_1Pt_1	0.522	0.806
Core-Shell: Au@Pd_1Pt_3	0.536	0.568

Table 4.1 CO peak position and the corresponding surface area.

Figure 4.4 shows the CO peak potential of all alloy and core-shell nanparticles, including Au@Pt and Au@Pd core-shell structures. Although Pd_3Pt_1 alloy and Pd_3Pt_1 alloy-shell core-shell nanoparticles have the CO stripping potentials closer to Au@Pd, Pd_1Pt_1 alloy composition has lower CO stripping potential than Pd_1Pt_3 alloy composition.

All the CO stripping peaks for PdPt alloy and Au@PdPt core-shell nanoparticles were located in between Au@Pt and Au@Pd, indicating the surface of the catalyst is alloy of platinum and palladium. It is found that the CO stripping peak position depends on the alloy composition and not related whether it has a gold core inside or not. Slight difference can be seen, but alloy and core-shell structures which have the same platinum and palladium alloy composition tend to have a close CO stripping peak position.

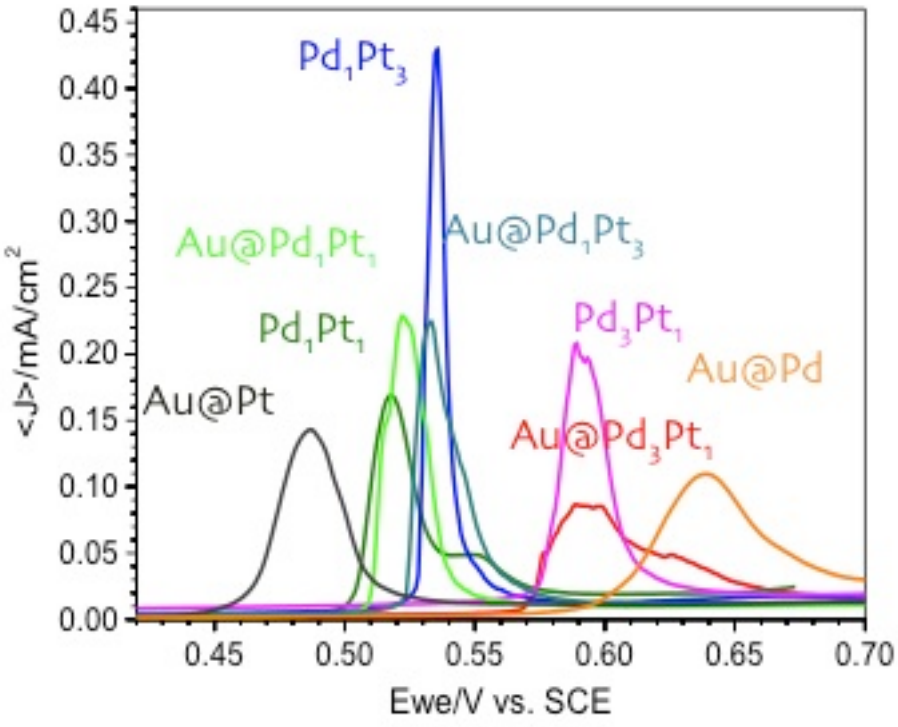

Figure 4.4 CO stripping peaks for PdPt alloy and Au@PdPt core-shell nanoparticles.

Based on the CO stripping results, the peak position was placed in relation to the PdPt alloy composition in Figure 4.5. Taking the palladium component as a x-axis and the CO stripping peak position as a y-axis, all alloy and core-shell nanoparticles including Au@Pd and Au@Pt were labeled. It could be seen that the CO stripping peak position does depend on the alloy composition, rather than the presence of gold core inside. As Figure 4.5 shows, there is a tendency that if the particle has more palladium component than that of platinum, the CO stripping peak position goes to higher potential. Interestingly, Pd_1Pt_1 composition appeared at the lowest peak potential for both PdPt alloy and Au@PdPt core-shell nanoparticles although Pd_1Pt_3 alloy composition was expected to have the lowest peak potential.

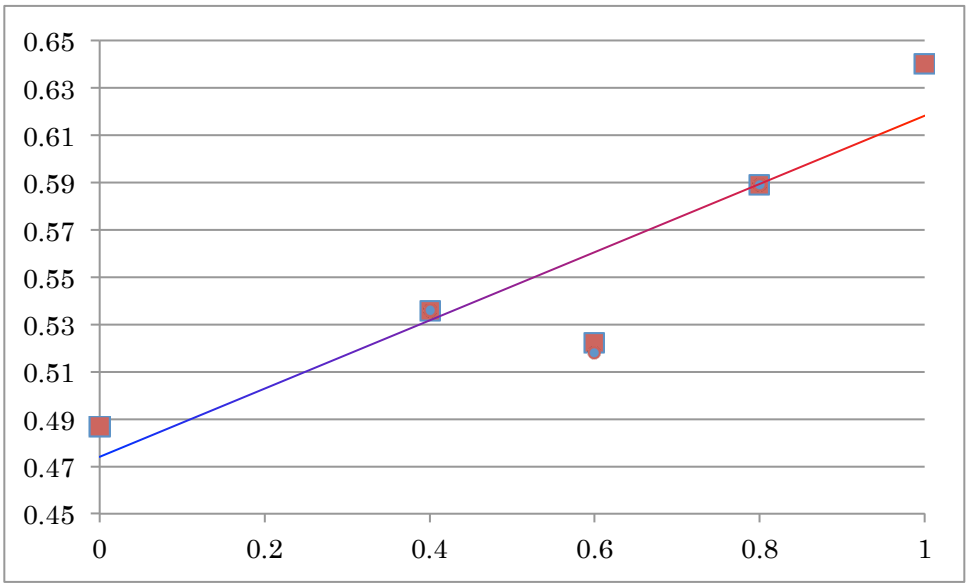

Figure 4.5 The linear relationship between PdPt alloy composition and the CO stripping peak position. (x=0.4 is Pd_1Pt_3, x=0.6 is Pd_1Pt_1, and x=0.8 is Pd_3Pt_1 alloy composition)

4.2.3 Formic Acid Oxidation

The electrocatalytic activity toward the oxidation of formic acid was investigated for each PdPt alloy and Au@PdPt core-shell octahedral nanoparticle. As shown in Figure 4.6, the indirect pathway is dominant for all the electrocatalysts, which means the specific formic acid oxidation peak can be obtained during the back scan. During the forward scan, formic acid is oxidized but at the same time the poisoning intermediate, carbon monoxide, is produced so that the overall formic acid oxidation is hindered. As the potential goes higher, the surfactants and the impurities on the catalyst surface are oxidized which is known as anodic peak, then the back scan proceeds. Since the surface of the catalyst is now much cleaner, a high oxidation peak is achieved.

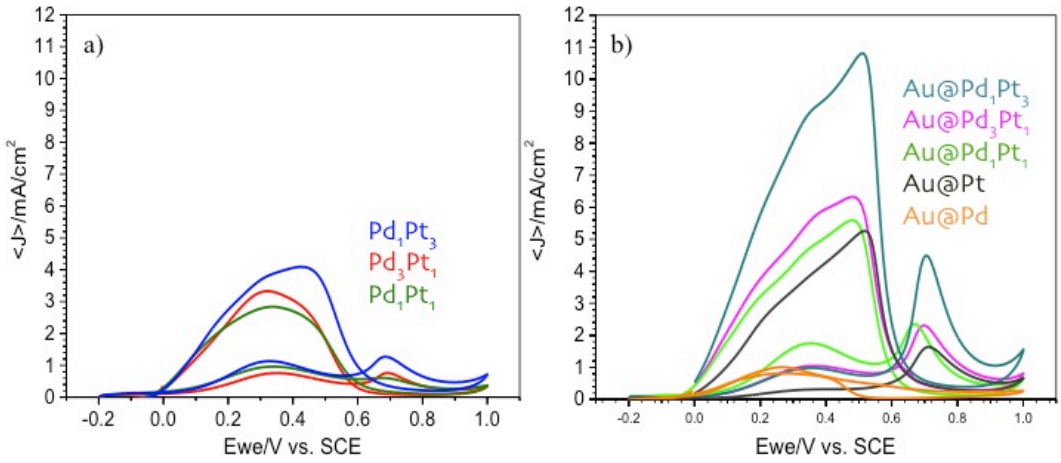

Figure 4.6 Cyclic voltammograms for the formic acid oxidation of a) PdPt alloy and b) Au@PdPt core-shell octahedral nanoparticles.

Table 4.2 summarizes the catalytic activity in the form of current density, current normalized by its surface area, for the formic acid oxidation of all alloy and core-shell nanoparticles.

Electrocatalyst	Current Density (mA/cm^2)
Alloy: Pd_3Pt_1	3.33
Alloy: Pd_1Pt_1	2.84
Alloy: Pd_1Pt_3	4.09
Core-Shell: Au@Pd_3Pt_1	6.32
Core-Shell: Au@Pd_1Pt_1	5.59
Core-Shell: Au@Pd_1Pt_3	10.96

Table 4.2 The list of FOR activity for PdPt alloy and Au@PdPt core-shell octahedral nanoparticles.

As Figure 4.7 demonstrates, the electrocatalytic activity toward the oxidation of formic acid can be seen in both PdPt alloy and Au@PdPt core-shell octahedral nanoparticles. The catalytic performance depends on the PdPt alloy composition. For the PdPt alloy composition, the highest catalytic activity was always achieved by Pt-rich composition, followed by Pd-rich and PtPd-even compositions. Moreover, Au@PdPt core-shell structures showed almost twice the activity than pure PdPt alloy nanoparticles, indicating the importance of the gold core. The gold core is considered to affect the catalytic activity by changing the electronic structure at the interface between the core and the shell as well as the particle surface, which leads to the difference in reaction preference.

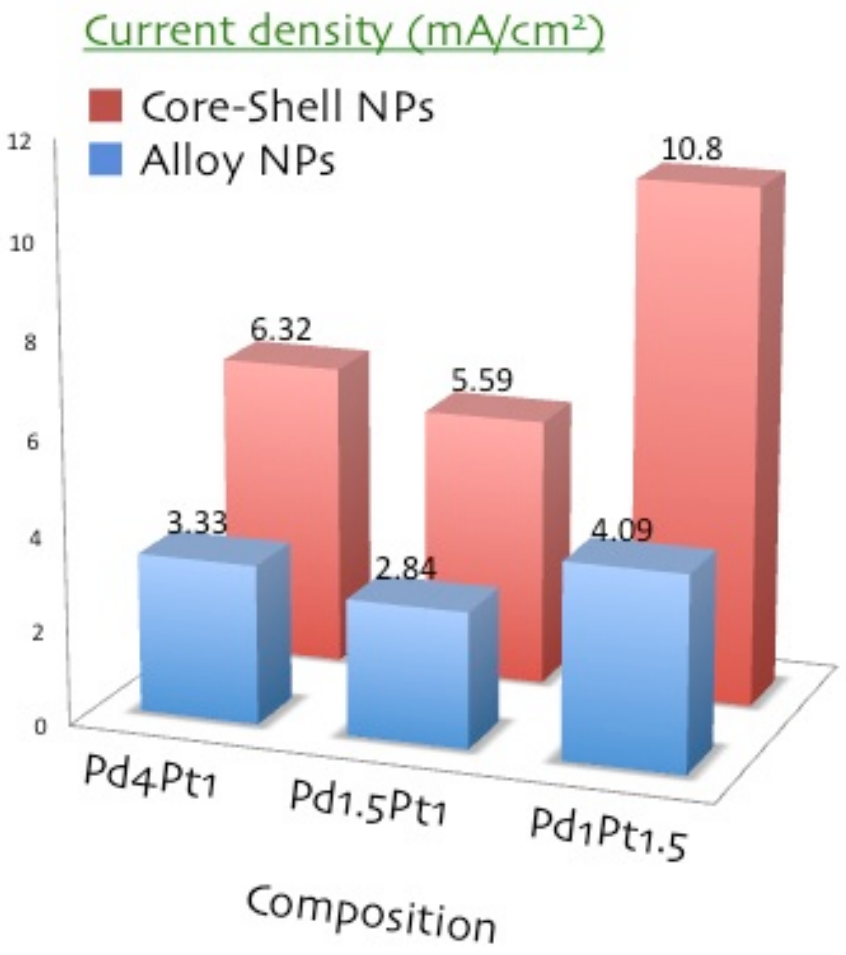

Figure 4.7 Formic acid oxidation activity summary for PdPt alloy and Au@PdPt core-shell octahedral nanoparticles with three alloy compositions.

CHAPTER 5

Discussion

5.1 Thinner shell: core1shell10 (C1S10) → core1shell2 (C1S2)

Figure 5.1 reports that the electrocatalytic activity toward the oxidation of formic acid is greatly enhanced when Au@PdPt core-shell octahedral nanoparticle is applied. From the XRD profile, the lattice expansion/contraction of Au@PdPt core-shell nanoparticles induced by the presence of the gold core could be observed. The original synthetic procedure set the core to alloy-shell as 1:10. In order to elucidate the effect of the gold core, the core to alloy-shell ratio was varied to 1:2 because a thinner alloy-shell would have a greater effect from the gold core.

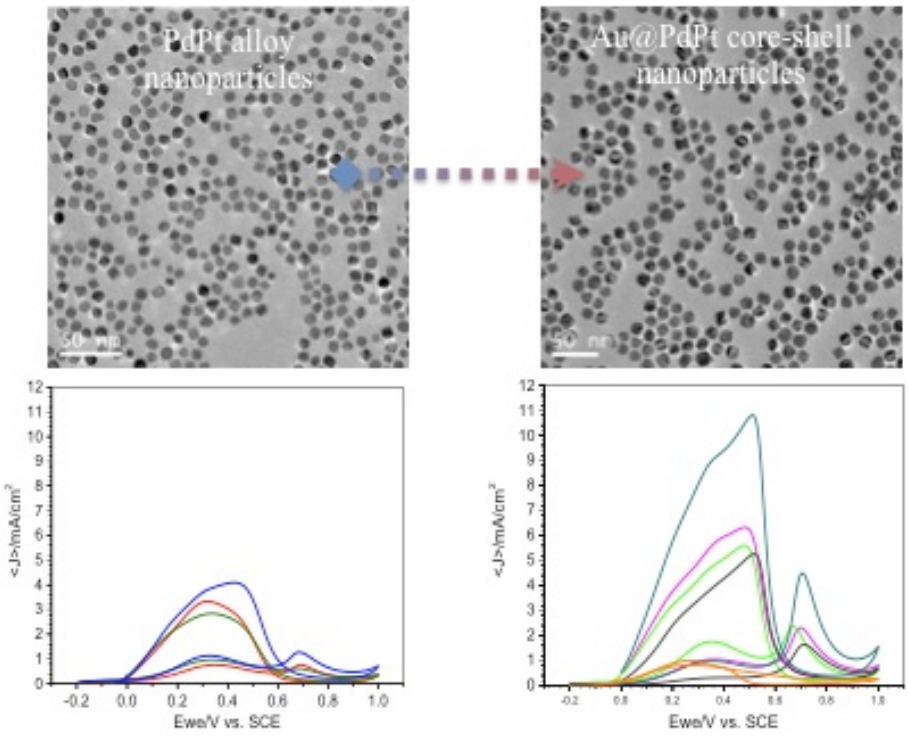

Figure 5.1 TEM images and their corresponding FOR activity of PdPt alloy and Au@PdPt core-shell octahedral nanoparticles.

5.1.1 Characterization of C1S2 Au@PdPt Core-shell Nanoparticles

The thinner shell C1S2 Au@PdPt core-shell nanoparticles were synthesized following the same procedure as the original Au@PdPt core-shell octahedral nanoparticle synthesis, but with the increased amount of gold seeds. In a typical synthesis for C1S2 Au@PdPt core-shell nanoparticle, 15 mL gold seeds solution was added into the growth solution. Figure 5.2 shows the representative TEM images for the C1S2 Au@PdPt octahedral nanoparticles with three different alloy-shell compositions. They are uniform and monodispersed. The averaged size is around 15 nm. The morphology of the particles is octahedral shape, but less-defined than C1S10 Au@PdPt core-shell nanoparticles.

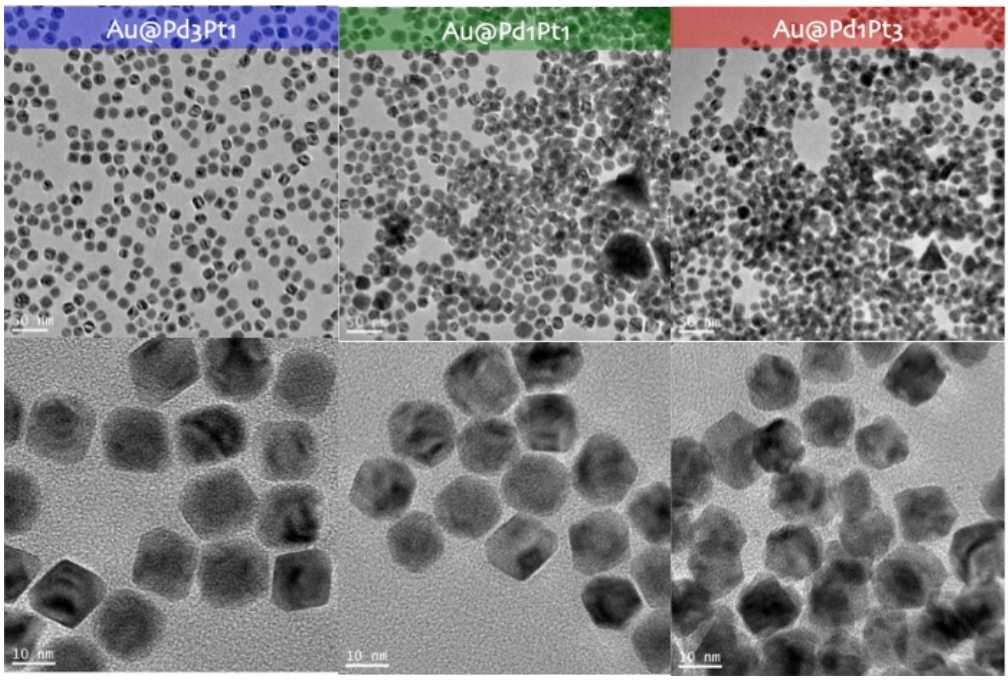

Figure 5.2 TEM images for thinner alloy-shell (C1S2) Au@PdPt core-shell octahedral nanoparticles with three different alloy-shell compositions.

The elemental composition of PdPt alloy-shell was determined by ICP-OES. (Table 5.1) The results matched well with what it should be.

Expected	ICP-OES
Pd_3Pt_1	$Pd_{2.739}Pt_1$ ($Pd_{2.7}Pt_1$)
Pd_1Pt_1	$Pd_{1.160}Pt_1$ ($Pd_{1.2}Pt_1$)
Pd_1Pt_3	$Pd_1Pt_{1.713}$ ($Pd_1Pt_{1.7}$)

Table 5.1 ICP-OES results for PdPt alloy-shell of C1S2 Au@PdPt core-shell octahedral nanoparticles.

5.1.2 Electrochemical Measurement Results

The CO stripping was measured using the core1shell2 Au@PdPt octahedral nanoparticles. As Figure 5.3 shows, all the CO stripping peak positions appeared in a higher potential region than those of C1S10 Au@PdPt octahedral nanoparticles. The peak positions were 0.536 V, 0.540 V and 0.560 V, and 0.681 V for C1S2 $Au@Pd_1Pt_1$, $Au@Pd_1Pt_3$, and $Au@Pd_3Pt_1$ nanoparticles respectively. The trend that $Au@Pd_1Pt_1$ has the lowest CO stripping potential can be still seen in the C1S2 Au@PdPt nanoparticles.

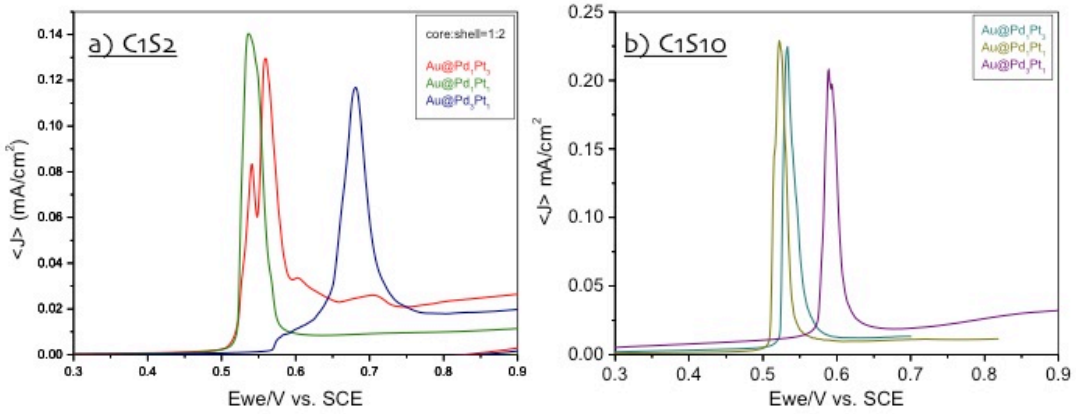

Figure 5.3 CO stripping cyclic voltammograms for a) C1S2 and b) C1S10 Au@PdPt core-shell octahedral nanoparticles.

The catalytic activity toward the formic acid oxidation was also examined for the C1S2 Au@PdPt core-shell octahedral nanoparticles. Although more enhanced catalytic activity was expected from the thinner alloy-shell core-shell structures due to its bigger effect from the gold core, Figure 5.4 shows that thinner alloy-shell C1S2 Au@PdPt core-shell octahedral nanoparticles are less active than C1S10 Au@PdPt core-shell octahedral nanoparticles and slight more active than PdPt alloy nanoparticles. The current density was measured as 5.65 V, 3.09 V and 2.47 V for C1S2 Au@Pd_1Pt_3, Au@Pd_3Pt_1 and Au@Pd_1Pt_1 core-shell nanoparticles respectively. The trend that Pd_1Pt_3 alloy-shell has the highest activity followed by Pd_3Pt_1 and Pd_1Pt_1 could be still observed.

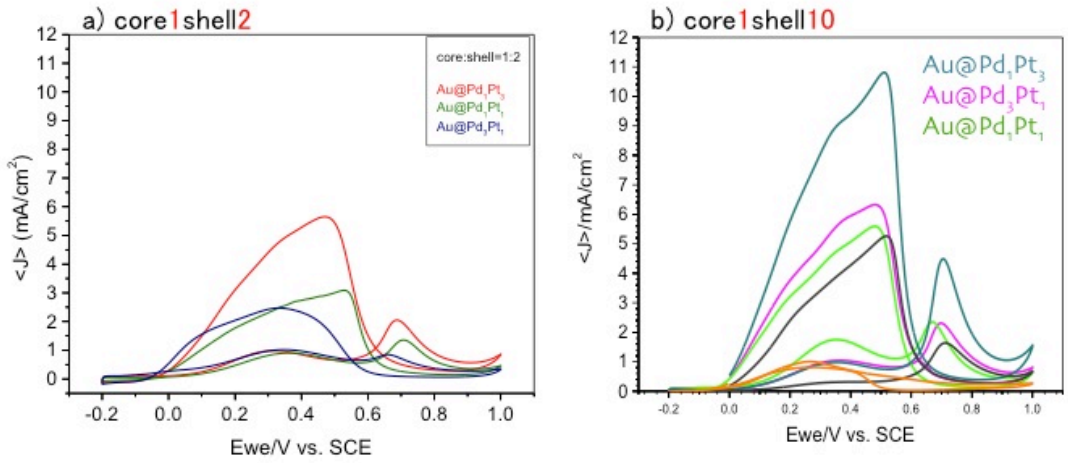

Figure 5.4 FOR activity comparison of a) C1S2 and b) C1S10 Au@PdPt core-shell octahedral nanoparticles.

Figure 5.5 summarizes all the electrochemical results, including PdPt alloy, C1S10 Au@PdPt core-shell and C1S2 Au@PdPt core-shell nanoaprticles. The z-axis

(height) is the catalytic activity (current density j) with the unit of mA/cm^2 and traverse axes are particles with/without cores of different compositions and alloy-shell thickness. The PdPt alloy-shell of C1S10 Au@PdPt core-shell particles should be relatively thicker and of C1S2 Au@PdPt core-shell particles should be thinner. Surprisingly, it is found there is a volcano-curve trend in catalytic activity from pure PdPt alloy to Au@PdPt core-shell nanoparticles with decreasing the thickness of alloy-shell.

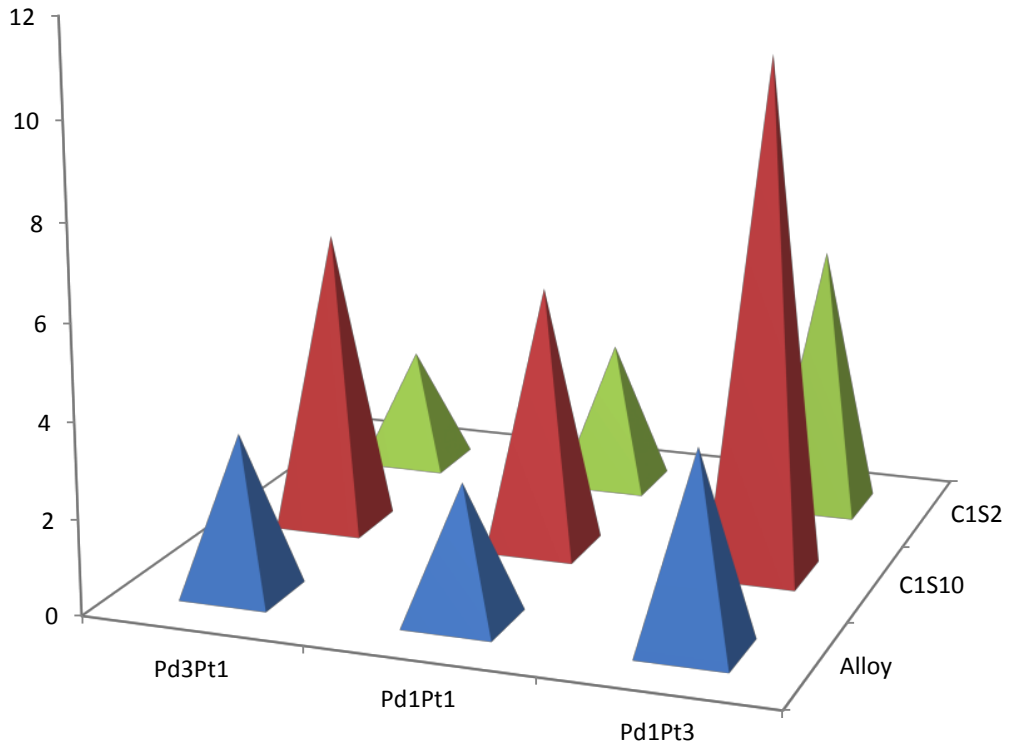

Figure 5.5 A chart to compare the FOR activity of PdPt alloy, C1S10 Au@PdPt core-shell and C1S2 Au@PdPt core-shell nanoparticles with three different PdPt alloy compositions.

5.1.3 XRD (220) Pattern Analysis

To elucidate this volcano-curve phenomenon, XRD (220) patterns of C1S2 Au@PdPt core-shell nanoparticles were analyzed in relation to those of PdPt alloy and C1S10 Au@PdPt core-shell nanoparticles. Figure 5.6 shows the XRD (220) patterns of PdPt alloy and C1S10 Au@PdPt core-shell nanoparticles with three different alloy compositions. It is easily understood that PdPt alloy-shell peak of C1S10 core-shell particles shifted from those of pure PdPt alloy nanoparticles, indicating there exists more lattice strain in the core-shell nanoparticles.

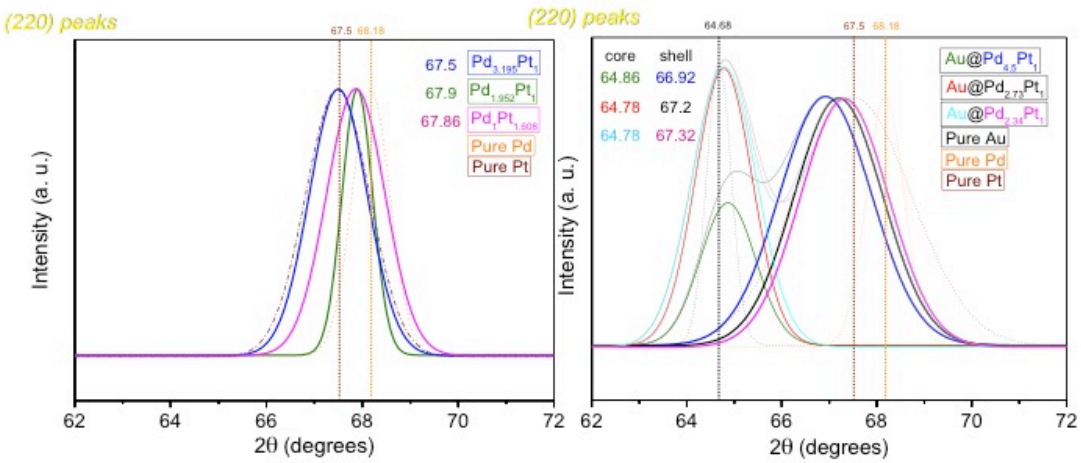

Figure 5.6 XRD (220) patters of PdPt alloy (Left) and C1S10 Au@PdPt core-shell (Right) octahedral nanoparticles.

In comparing the XRD (220) peaks of C1S10 and C1S2 Au@PdPt core-shell nanoparticles for each PdPt alloy-shell composition (Figure 5.7), the peaks of C1S2 thinner alloy-shell always shift more than those of C1S10 thicker alloy-shell. This demonstrates that thinner alloy-shell undertakes stronger lattice strains than thicker

alloy-shell, which means there is a linear relationship between the thickness of alloy-shell and the strength of lattice strains. Interestingly, no significant peak shift was observed in gold core, indicating the lattice change in PdPt alloy-shell is induced from the core.

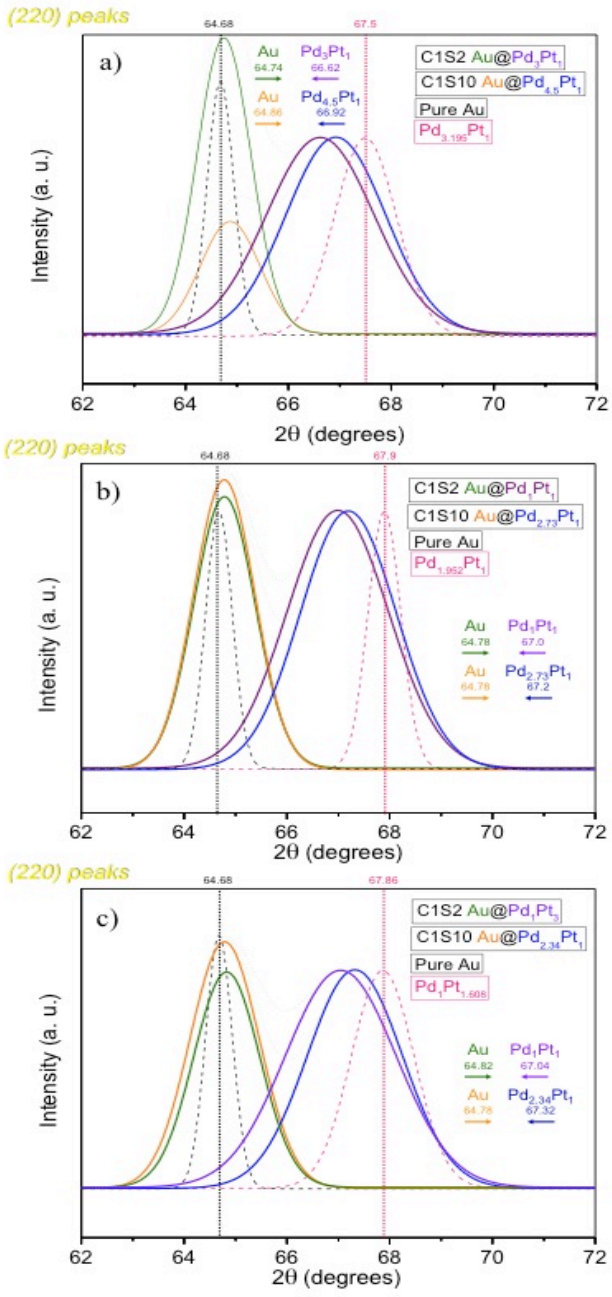

Figure 5.7 XRD (220) pattern comparisons of each PdPt alloy-shell of C1S2 and C1S10 Au@PdPt core-shell nanoparticles: a) Pd_3Pt_1 b) Pd_1Pt_1 c) Pd_1Pt_3 alloy-shell.

Since the d-space is inversely proportional to the peak angle, the XRD (220) analysis data indicate that the d-space of the PdPt alloy-shell becomes much larger. Table 5.2 shows the d-space values for Pd_1Pt_1 alloy-shell in C1S10 and C1S2 Au@PdPt core-shell octahedral nanoparticles get larger than pure PdPt alloy nanoparticles, whereas no significant difference could be seen in Au core d-space length. Scheme 5.1 illustrates the lattice length of PdPt alloy-shell is greatly expanded, while that of Au core has almost no change.

	Au seeds	PdPt alloy	C1S10 Au@PdPt	C1S2 Au@PdPt
Au core	1.438	N/A	1.439	1.439
PdPt alloy-shell	N/A	1.380	1.386	1.396

Table 5.2 The d-space value changes of Pd_1Pt_1 alloy-shell in C1S10 and C1S2 Au@PdPt core-shell octahedral nanoparticles.

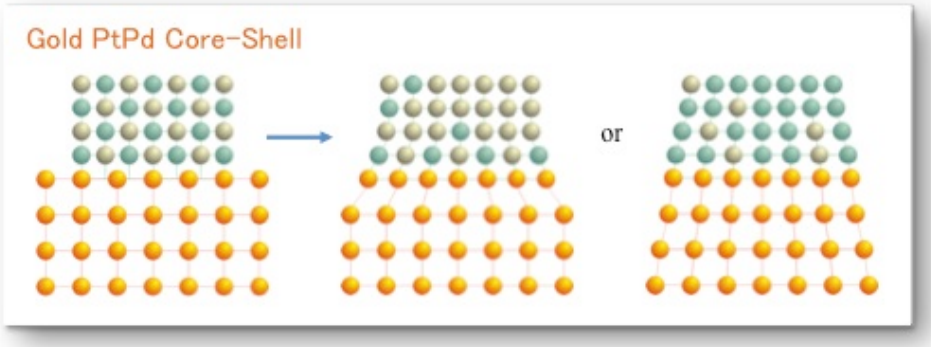

Scheme 5.1 Schematic illustration of lattice expansion of PdPt alloy-shell in Au@PdPt core-shell octahedral nanoparticles.

5.2 The Effect of Lattice Strain for Catalytic Activity

Figure 5.8 demonstrates the electrochemical activity toward formic acid oxidation of C1S10 Au@PdPt core-shell nanoparticles is higher than that of C1S2 Au@PdPt core-shell nanoparticles which have stronger lattice strain. Based on this outcome, it could be proposed that a best strength of lattice strain should exist, making a volcano curve for electrochemical activity toward the oxidation of formic acid. When the strength of lattice strains get too large or too small, which means the alloy-shell get too thick or too thin, the enhanced surface activity of alloy-shell would be diminished. It is highly suggested that the lattice strain on the interface between gold core and PdPt alloy-shell induces the corresponding lattice contraction/expansion to both gold core and PdPt alloy-shell, which further changes the electronic property on the surface and results in the improvement of its catalytic activity.

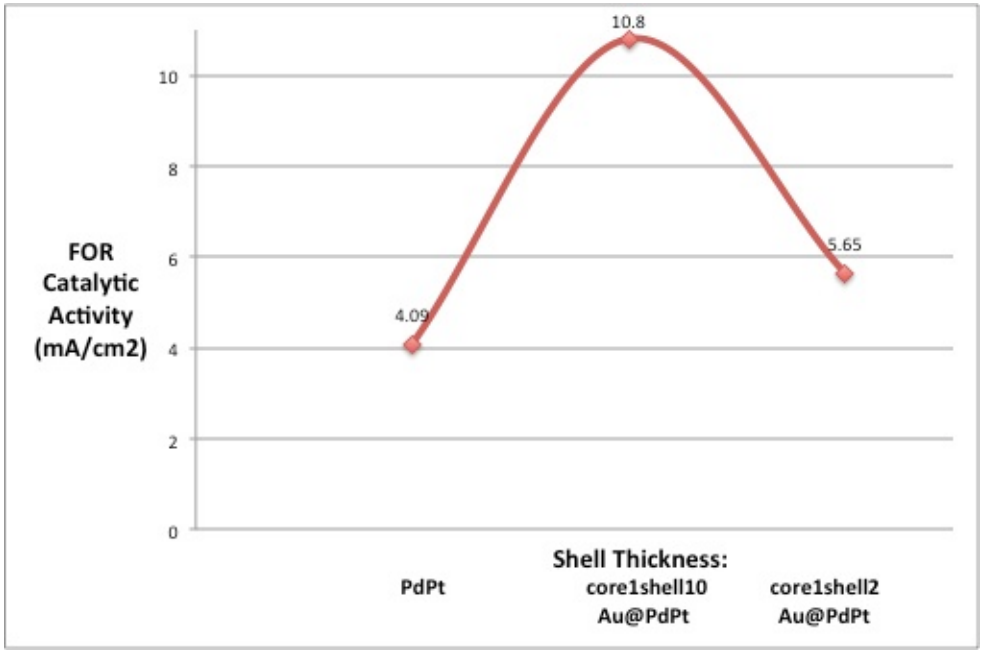

Figure 5.8 Volcano-curve relationship between the FOR catalytic activity and the alloy-shell thickness.

CHAPTER 6

Conclusion

PdPt alloy and Au@PdPt core-shell octahedral nanoparticles were successfully synthesized by a simple hydrothermal method in aqueous system. The octahedral particles were single crystalline and uniformly monodispersed. The PdPt alloy particle size is ~7 nm and the Au@PdPt core-shell particle size is ~18 nm. Both the size and morphology of alloy and core-shell particles could be well controlled. The particles were characterized by TEM, HRTEM, EDS, ICP-MS and XRD to confirm their shape, alloy nature, and core-shell structure. It is proposed that the key conditions for producing sub-20 nm size octahedral PdPt alloy and Au@PdPt core-shell particles are the usage of mild reducing agent and the amount of oxygen in the growth solution.

The catalytic performance of octahedral PdPt alloy and Au@PdPt core-shell particles toward formic acid oxidation was examined. Both alloy and core-shell particles showed very promising catalytic activities. Two interesting points could be observed. First, Pt-rich alloy composition always achieved the highest catalytic activity in octahedral PdPt alloy and Au@PdPt core-shell particles. Secondly, the Au@PdPt core-shell particles were twice as active as their PdPt alloy counterparts.

The relationship between the alloy-shell thickness and the catalytic activity was studied based on the XRD (220) pattern analysis. It is found that there exists a volcano-curve for the catalytic performance, which could be explained in terms of the lattice strain induced by gold core on the interface between core and shell as well as on the surface.

In the future, the synthesis of other core to alloy-shell ratios such as core1shell1

and core1shell20 Au@PdPt core-hell octahedral particles will be carried out. Having more data would further support our volcano-curve performance graph explanation in relation to the alloy-shell thickness and the catalytic activity. What is expected to see is core1shell1 has lower catalytic activity and core1shell20 might have either higher or lower catalytic activity than core1shell10 Au@PdPt core-shell nanoparticles. In addition, the catalytic performance of PdPt alloy and Au@PdPt core-shell octahedral nanoparticles toward other fuel cell reactions, in particular oxygen reduction reaction (ORR) will be tested. It has been known that for the face-centered cubic (fcc) alloy and core-shell system, octahedral or tetrahedral nanocrystals are desirable because they are all enclosed by (111) facet that is the most active crystal facets toward ORR. Thus, octahedral PdPt alloy and Au@PdPt core-shell nanoparticles would be promising candidates as an ORR catalyst.